2020

Ab Initio Modeling of an Electron Transport Layer Interface in Hybrid Perovskite Solar Cells

Krantikumar Subhash Pawar
Wright State University

AB INITIO MODELING OF AN ELECTRON TRANSPORT LAYER INTERFACE IN HYBRID PEROVSKITE SOLAR CELLS

A Thesis submitted in partial fulfilment of the
requirements for the degree of
Master of Science in Materials Science and Engineering

By

KRANTIKUMAR SUBHASH PAWAR
B.E., Shivaji University, India, 2015

2020
Wright State University

WRIGHT STATE UNIVERSITY
GRADUATE SCHOOL

Nov 30,2020

I HEREBY RECOMMEND THAT THE THESIS PREPARED UNDER MY SUPERVISION BY Krantikumar Subhash Pawar ENTITLED "Ab Initio Modeling of an Electron Transport Layer Interface in Hybrid Perovskite Solar Cells" BE ACCEPTED IN PARTIAL FULFILLMENT OF THE REQUIREMENTS FOR THE DEGREE OF Master of Science in Materials Science and Engineering.

_____
Amir A. Farajian, Ph.D.
Thesis Director

_____
Raghavan Srinivasan, Ph.D., P.E.
Chair, Department of
Mechanical and Materials
Engineering

Committee on Final Examination:

_____
Amir A. Farajian, Ph.D.

_____
Raghavan Srinivasan, Ph. D., P.E.

_____
James A. Menart, Ph. D.

_____
Barry Milligan, Ph.D.
Interim Dean of the Graduate School

ABSTRACT

Pawar, Krantikumar Subhash, M.S.R.C.E.E. Department of Mechanical and Materials Engineering. Wright State University 2020. Ab Initio Modeling of an Electron Transport Layer Interface in Hybrid Perovskite Solar Cells.

Hybrid organic-inorganic perovskite solar cell is an emerging technology which has shown the fastest advancement in power conversion efficiency within a few years since introduction, thus making it one of the clean energy breakthroughs. These cells are based on thin-film technology which makes them suitable to manufacture using low-cost solution processing methods. As these types of cells are easily tunable with the selection of different materials, interfacial engineering is an important approach to increasing their efficiency. One of the main hurdles in this regard is the loss caused by the recombination of separated charges. An approach to tackle these issues is to incorporate organic monolayers between the charge (electron/hole) transport layers and the perovskite active layer. Such interface engineering has experimentally shown to improve the overall efficiency and stability of the cell. The current research focuses on the study of TiO_2/HOOC-Ph-SH interface in order to understand the improved efficiency. Using ab initio quantum mechanical approach, we investigate the monolayer (HOOC-Ph-SH) adsorption onto the TiO_2 surface to determine structural and electronic properties of the interface and discuss the connection of the results to solar cell performance.

TABLE OF CONTENTS

LIST OF FIGURES

FIGURE **PAGE**

LIST OF TABLES

LIST OF ABBREVIATIONS

CdTe	Cadmium Telluride
CIGS	Copper Indium Gallium Selenide
DSSC	Dye-Sensitized Solar Cells
$CH_3NH_3PbI_3$	Methyl Ammonium Lead Iodide
$MAPbI_3$	Methyl Ammonium Lead Iodide
PSCs	Perovskite Solar cells
NREL	National Renewable Research Laboratory
ETL	Electron Transport Layer
HTM	Hole Transport Material
FTO	Fluorine Doped Tin Oxide
CuSCN	Copper Thiocyanate
ELF	Electron Localization Function
PDOS	Partial Density of States
PCE	Power Conversion Efficiency
MBA	4-Mercaptobenzoic acid
HOMO	Highest Occupied Molecular Orbital
HOOC-Ph-SH	4-mercaptobenzoic acid
PVCz	Poly (Vinyl Carbazole)

HOMO	Highest Occupied Molecular Orbital
LUMO	Lowest Occupied Molecular Orbital
HS-PhF_5	Pentafluoro benzenethiol
FAMA	Formamidinium Methylammonium
PCBM	[6,6]-phenyl C_{61} butyric acid methyl ester
FF	Fill Factor
TTC	Tetra tetracontane
HOOC-Ph-SH	4- Mercaptobenzoic acid
HS-C_6-F_5	Pentafluoro benzenethiol
VASP	Vienna ab initio Simulation Package
DFT	Density Functional Theory
LDA	Local Density Approximation
GGA	Generalized Gradient Approximation
PAW	Projector Augmented Wave
VESTA	Visualization for Structural and Electronic Analysis
TDOS	Total Density of States
CBM	Conduction Band Minimum
VBM	Valence Band Maximum

ACKNOWLEDGEMENTS

I would like to express my deep and sincere gratitude to my thesis advisor, Dr Amir A. Farajian for giving me the opportunity to carry out this research and providing invaluable guidance throughout. Completion of this work could not have been accomplished without his support and encouragement. The most important thing I learned from him is how not to overwhelm and approach the problem with different angles by taking small consistent steps.

I would like to thank all my committee members for their precious time and attention. I would like to thank Mike VanHorn for helping me with all kinds of computer-related issues. I would like to thank Luke Wirth for his guidance and support throughout the thesis. Also, I am thankful to Ohio supercomputers for providing me with the required resources to carry out my research.

Finally, I would like to thank my parents for their love and support throughout my career. Also, I am thankful to all my friends for being there for me in tough times.

CHAPTER 1 INTRODUCTION

1.1 Motivation

The Sun's energy enters into the earth atmosphere in the form of heat radiations and light rays. This source of green and abundant energy can be easily harvested for the generation of electricity in order to sustain traditional non-renewable resources. Solar energy is the result of fusion reactions taking place inside of the sun that generates heat and radiation, which can be easily converted into electricity with the help of solar photovoltaic technologies.

Perovskite as a solar cell material has been showing some interesting properties and higher power conversion efficiencies compared to the traditional mono and polycrystalline silicon solar cells. It took around 50 years of research and development for silicon solar cells to reach the current efficiency of 25 %. However, within several years of introduction, the perovskite solar cells have surpassed the 26 % efficiency in the laboratory. The perovskite solar cells are organic-inorganic types of cells which are more scalable and cost-effective as they are very easy to manufacture by low-cost solution processing methods compared to traditional solar cells which have high manufacturing costs.

They are based on thin-film technology which reduces the amount of material required for fabrication and makes them lightweight and flexible. They are versatile and can be used in other sites of the building besides the roof panels. Based on these properties they have the potential to replace the traditional solar cells and become the next generation of solar cell material. Currently, research allows these cells to be used in combination with

other solar cell materials such as silicon and CIGS solar cells, these combined cells are called as 'Tandem cells'.

Despite having all these advantages over the traditional solar cells, the stability issues prevent these cells from being used commercially. They are easily degraded in external environmental conditions due to attack of air and moisture. Also, they face recombination losses due to trap states. Current research in the field is focused on removing these roadblocks to improve the overall cell performance such that they are ready to be used commercially.

Jing Cao and his team recently published a paper in 2015, which depicts the idea of using thiols as an interfacial modifier in hybrid perovskite solar cells which have experimentally proved to improve the overall stability and efficiency of the cell [14]. The motivation for this thesis came from his work, to investigate further the reasons showing the improved performance using an atomic simulation approach. Here we analyze the interface of thiol monolayer (4-mercaptobenzoic acid) and TiO_2 using various simulation tools to understand various electronic and structural properties of the perovskite solar cell.

1.2 Introduction to solar cell

A solar cell is a device which converts solar energy into electricity by using the phenomenon called the photovoltaic effect. Alexandre Edmond Becquerel first observed this phenomenon in 1839 while working with an electrochemical cell, and the first silicon solar cell was created by bell laboratories in 1954. A solar cell is made from a semiconductor material, which absorbs the photon energy coming from the Sun to produce charge carriers (electrons and holes) that generate electricity. The incident photons with

energy higher than the bandgap energy of semiconducting material are absorbed by the electrons in the valence band, and these excited electrons jump into the conduction band. This creates electron-hole pairs in the semiconducting material, which move in the opposite direction and result in potential difference across the cell eventually generating electricity [1].

1.3 Types of solar cell technologies

The solar PV cells can be classified in the following categories based on materials and technology used [2]. The first-generation of solar cells are based on wafer-based silicon material, which provides high power conversion efficiency with great stability, and therefore are widely used. Around 90% of the current solar panels are made from the silicon-based cells. They fall into two subcategories based on the structure of the material used, such as mono and polycrystalline silicon solar cells. Monocrystalline silicon cells are produced in single crystals by the process of recrystallization which is expensive but provides high efficiency of around 17%-18%. Polycrystalline silicon cells are more economical as they are made from different crystals connected in a single cell which makes their manufacturing less expensive. However, they have less efficiency (12%-14%) compared to monocrystalline silicon cells [2].

Second-generation of solar cells are mainly based on thin-film technology. They consist of amorphous silicon, CdTe and CIGS solar cells. Amorphous silicon solar cells are manufactured with low-cost methods as they don't have a specific arrangement of atoms compared to the crystalline silicon cells. However, they suffer from unstable efficiency which falls in the range of 4% to 8%. CIGS solar cells are very popular due to

their low-cost manufacturing methods and direct band light absorption. They are highly stable and show efficiency around 10%-12% which makes them one of the best thin-film solar cell technology. In the case of CdTe cells, cadmium is a heavy metal considered toxic for the environment thus their use is limited [2].

Third-generation solar cells use novel evolving technologies. Some of the main types are Nano crystal-based, polymer-based, dye-sensitized and concentrated solar cells. Quantum dots are used in nanocrystal based solar cells in place of semiconducting material. Polymer-based solar cells are made from organic material in which combinations of donor polymer and acceptor fullerene materials are used. They provide special properties such as flexibility, semitransparency and lightweight. Also, they are highly scalable for commercial use.

Dye-sensitized solar cells are produced from dye materials placed between the different electrodes. They are highly flexible, transparent and cost-effective which can be produced by the simple fabrication methods like printing techniques. Concentrated PV solar cells collect the sun rays with the help of lens and mirror at a single region on the solar PV module to get the high intensity of solar energy. Perovskite-based solar cells can reach efficiency unto 31% [2].

CHAPTER 2 LITERATURE REVIEW

2.1 Perovskite as a solar cell material

Perovskite-based materials have a general formula of ABX_3 and structure similar to that of perovskite mineral that is how they got the name perovskite. The crystal structure of the perovskite molecule is shown in Fig. 2.1, here, 'B' is a smaller cation positioned at the center, 'A' is another larger cation, and a halogen atom 'X' is positioned at each face of the unit cell. There are many possible varieties of perovskite materials depending upon the combination of the cation, anion and halides used. The most common perovskite solar cell consists of methyl-ammonium ($CH_3NH_3^+$) as an organic cation, 'Pb' as an inorganic cation and 'X' as halogen atoms such as I, Cl and Br. Choice of the different combination of atoms influences various properties of these types of solar cells, such as bandgap, diffusion of atoms, mobility, absorbance etc. Methyl-ammonium lead iodide ($CH_3NH_3PbI_3$) is the most widely used perovskite material for solar cell application because of its high efficiency and is commonly denoted by $MAPbI_3$, where 'MA' stands for methyl-ammonium.

Perovskite materials have a wide range of properties which make them suitable for solar cell applications. They have a direct bandgap which covers the entire range of visible spectrum leading to high light absorbance. Also, the bandgap is readily tunable in the range of 1.4 – 2.3 eV with a different combination of doped halides which makes them suitable for a wide range of solar applications. They have excellent defect tolerance properties which makes them easy to manufacture with low-cost solution processing methods such as inkjet printing and spin-coating. They have long-range electron-hole transport properties

which reduce the recombination losses hence results in high overall efficiency. These dye manufacturing methods make it possible for them to be made as thin, flexible and semi-transparent films. The material required for PSCs to absorb the same amount of the sunlight is 20 times less than the amount needed for silicon cell.

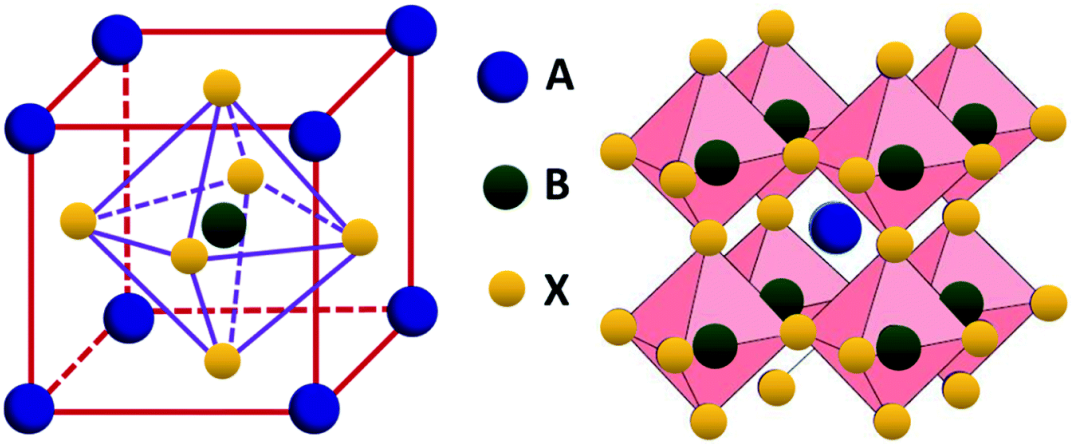

Figure 2.1 Structure of Perovskite crystal

The significance of perovskite solar cell technology can be understood by observing the efficiency chart for most established highly efficient solar cell technologies available, obtained from NREL (National Renewable Energy Laboratory) shown in Fig. 2.2.

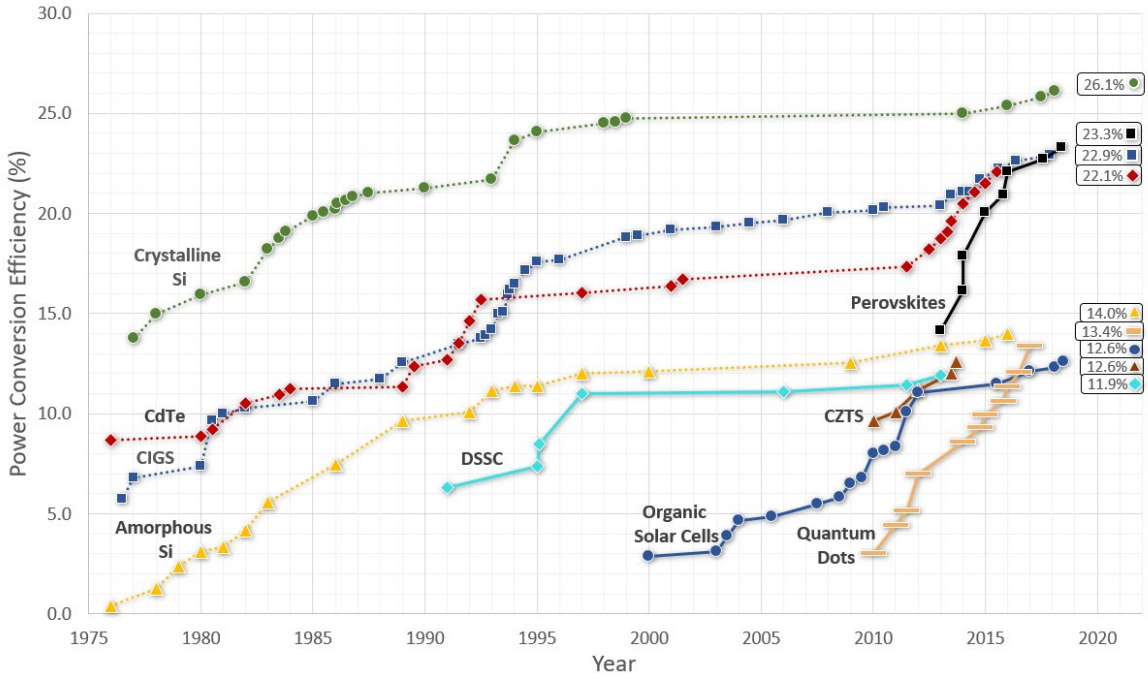

Figure 2.1 Power conversion efficiency of some of the most established highly efficient solar cell technologies available (Obtained from NREL)

The efficiency of the PSCs shows an exponential growth over a small-time (5 – 6 years) as compared to the other cell technologies such as CdTe, crystalline silicon and CIGS solar cells which have been available for more than 40 years. They have successfully surpassed the efficiency of other thin-film cell materials such as CdTe and CIGS and very close to surpass the crystalline silicon cells.

Despite having such high-power conversion efficiency, these emerging materials face various challenges. The biggest issue with these cells is their instability as they degrade in external environmental conditions such as moisture, oxygen and heat from sunlight. One of the inorganic constituents of the cell 'Pb' is considered as toxic material and may cause serious health issues, also lead is regarded as an environmental pollutant which is the breakdown byproduct of one of the perovskite-based cells. However, a very minuscule amount of lead is used in these cells (2mg/watt energy produced). Replacing the

'Pb' with 'Sn' can solve this problem although the original efficiency is not maintained. The other issue is the charge recombination caused by the accumulation of trap states at the ETL/perovskite/HTM interface, which limits their long-term performance.

2.2 Configuration of perovskite solar cells (PSCs)

PSCs are based on thin-film technology as they require a very thin layer of material ranging from few nanometers to tens of micrometers to generate electricity. The general cell configuration of one of the perovskite cells is shown in Fig. 2.3 a). In this case, FTO (Fluorine doped tin oxide) is used as a substrate material, which is placed on transparent glass. Mesoporous TiO_2 layer is deposited onto the substrate which acts as electron transport material. Perovskite material is the active light absorber layer which is placed onto mesoporous TiO_2 and after that copper thiocyanate (CuSCN) layer is deposited which acts as a hole transfer layer.

(a) (b)

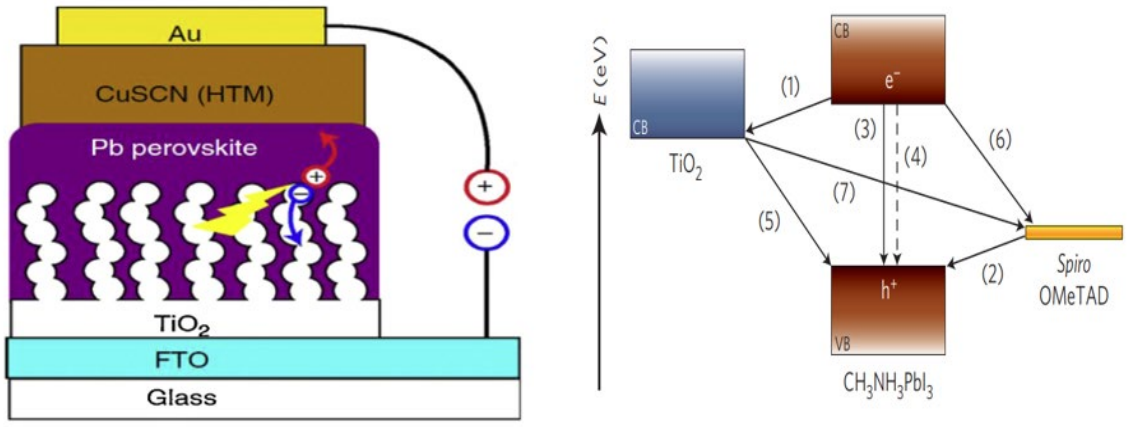

Figure 2.2 (a) Structure and (b) energy band diagram of $CH_3NH_3PbI_3$ perovskite cell [4]

Various types of HTMs and ETLs are being used for the fabrication of these cells; however, TiO_2 and Spiro-OMeTAD are the most commonly used as ETL and HTM materials due to their better performance. Various researchers are altering the combination of different materials to improve the overall efficiency and stability of these cells.

Fig. 2.3 b) shows the energy band alignment for the cell configuration in order to understand the desirable and undesirable charge transfer mechanisms. When the active perovskite layer absorbs incident sunlight, the photon energy is used to generate electron-hole pairs. The separated electrons are transferred to electron transfer layer TiO_2 and the holes are transferred to hole transfer material Spiro-OMeTAD. Path (1) shows the effective transfer of generated electrons to the TiO_2 and path (2) shows the effective hole transfer to the hole transfer material Spiro-OMeTAD. Whereas, the paths (3), (4), (5), (6) and (7) show all the possible ways of recombination of the separated charges across the interface. In order to get a better charge transfer across the interface, the generated electron and holes should be separated (processes (1) and (2)) before they get a chance of recombination both directly and indirectly. Therefore, the recombination processes corresponding to paths (from (3) to (7)) should be much slower.

2.3 Titanium Dioxide (TiO_2) as ETL

Titanium dioxide is widely used as ETL material for solar cell applications, as it provides effective contact for perovskite material that enhances electron injection and hole blocking [15]. It also provides mechanical support to the overall cell. Titanium dioxide mainly occurs in three major phases, namely brookite, anatase, and rutile [11]. Mainly rutile and anatase phases are widely used as they are more suitable for solar cell

applications. The crystal of rutile TiO_2 has a tetragonal structure with titanium atoms surrounded by six oxygen atoms as shown in Fig. 2.4. The unit cell parameters for construction purposes are taken from the literature [14] which are a = b = 4.594 Å ± 0.003 Å, c = 2.959 ± 0.002 Å, c/a = 0.6441. For the unit cell construction, titanium atoms are placed at the coordinates (0,0,0) and $(\frac{1}{2},\frac{1}{2},\frac{1}{2})$ and four oxygen atoms are placed at ± $(x, x, 0)$ and $\pm(\frac{1}{2}+x,\frac{1}{2}-x,\frac{1}{2})$ where x = 0.306 ± 0.001 [15]. Fig. 2.4 shows the crystal structure of rutile TiO_2 created using VESTA software.

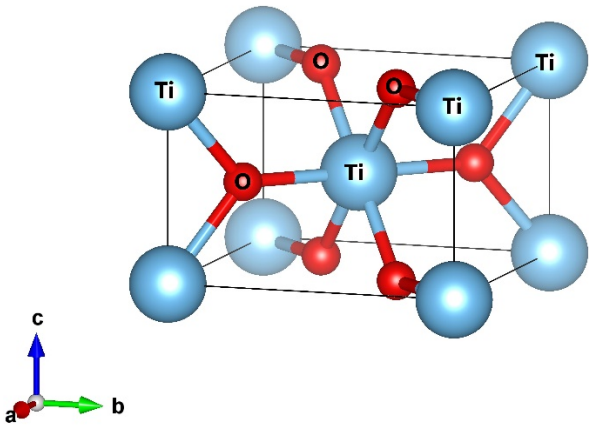

Figure 2.3 structure of rutile titanium dioxide [created using VESTA]

2.4 Perovskite/ TiO_2 interface in PSC

Understanding the interface between perovskite and TiO_2 is very essential to analyze the charge transfer mechanism and electronic properties at the interface. We have studied the literature published by Geng et al. in which they have analyzed the four different Interfaces with best lattice matching between the perovskite ($CH_3NH_3PbI_3$) and TiO_2 using first principle calculations [6]. Here, the tetragonal phase of the perovskite ($CH_3NH_3PbI_3$) is considered for all the first principle calculations. These perovskite cells occur in different phases depending on the temperature, including a tetragonal phase between 161K-330K

temperature range hence it is a stable phase at room temperature. The perovskite structure consists of alternate layers of PbI_2 and MAI (CH_3NH_3I) along Z-axis, therefore it is essential to consider both of these terminations while considering the adsorption with TiO_2. For TiO_2, both anatase (001) and rutile (001) phases are taken into consideration as they have a very small mismatch with the perovskite lateral dimensions.

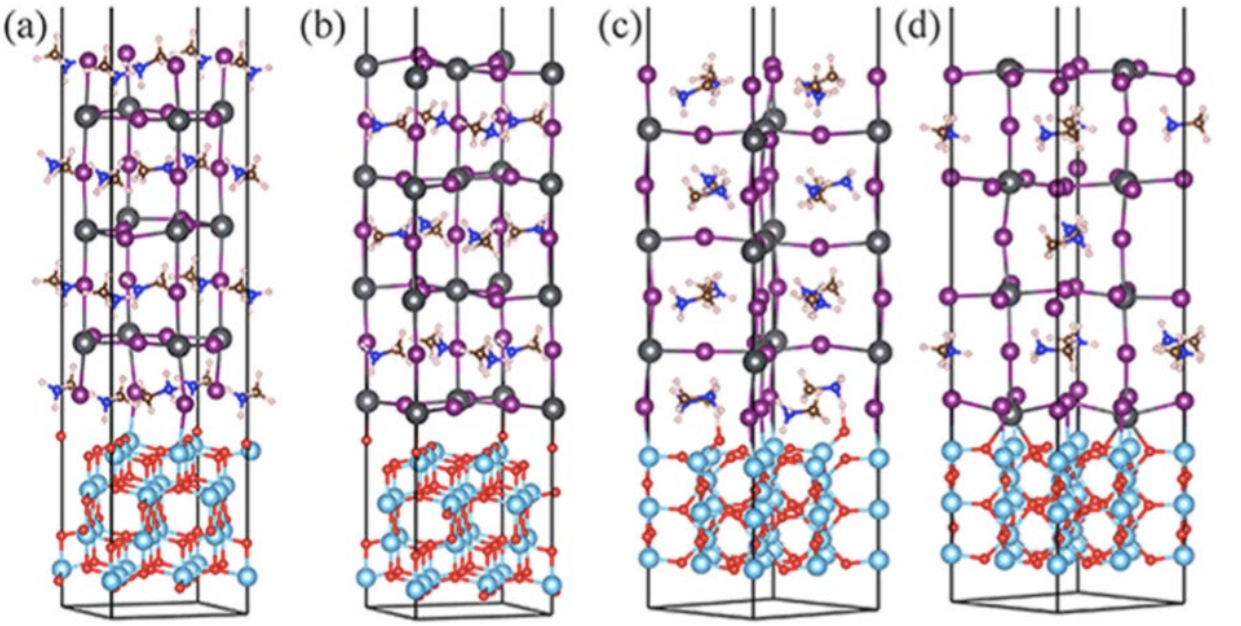

Figure 2.4 Perovskite/ TiO_2 interface (a) MAI/A (b) PbI/A (c) MAI/R (d) PbI/R [6]

Fig. 2.5 shows fully relaxed and optimized four possible interfaces formed between perovskite and TiO_2 as follows.

a) MAI-T/Anatase (MAI/A)

b) PbI_2-T/Anatase (PbI/A)

c) MAI-T/Rutile (MAI/R)

d) PbI_2-T/Rutile (PbI/R)

The interface formed between MAI terminated perovskite and anatase TiO_2 is shown in Fig. 2.5 a). At this interface, ionic/covalent bonding between 'I' and 'Ti' atoms is present with 50% bond formation among the interfacial atoms. Additionally, the interfacial 'O' atoms from TiO_2 breaks the bonds with Ti and attaches to 'H' forming 'O-H' bond, as determined by corresponding distances.

For PbI/A system shown in Fig. 2.5 b), there is a bond formation between 'I' and 'Ti' atoms, and 'Pb' and 'O' atoms. For MAI/R system shown in Fig. 2.5 c) there is same bond formation as that for MAI/A interface, except the bond lengths, are shorter and all the perovskite atoms involved with rutile interface are in chemical bonding compared to anatase phase, hence they provide better physical contact with perovskite termination.

For the PbI/R interface shown in Fig. 2.5 d), besides with 'Ti' and 'O' bonding, oxygen atoms are bonded with 'Pb' atoms forming 'O-Pb-O' bond without breaking bonds between 'TiO_2'. Also, they have a relatively shorter bond length compared to the anatase phase, which is the indication of stronger chemical bond formation.

The binding energy calculation supports the strong ionic/covalent bonding in all PbI terminated interfaces thus PbI terminated perovskite with rutile TiO_2 interface proved to have the highest binding energy amongst all the interfaces. At MAI terminated interfaces, the weak interaction between MA^+ and other ions is due to the Van der Waals bonding or hydrogen bonding. However, in PbI terminated interface the interaction of Pb^{2-} ions with TiO_2 is through ionic/covalent bonding, which makes them strongly attached. As binding energy is directly associated with the lattice matching, the binding energy of PbI/R is highest of all which makes it the most thermodynamically stable interface [6].

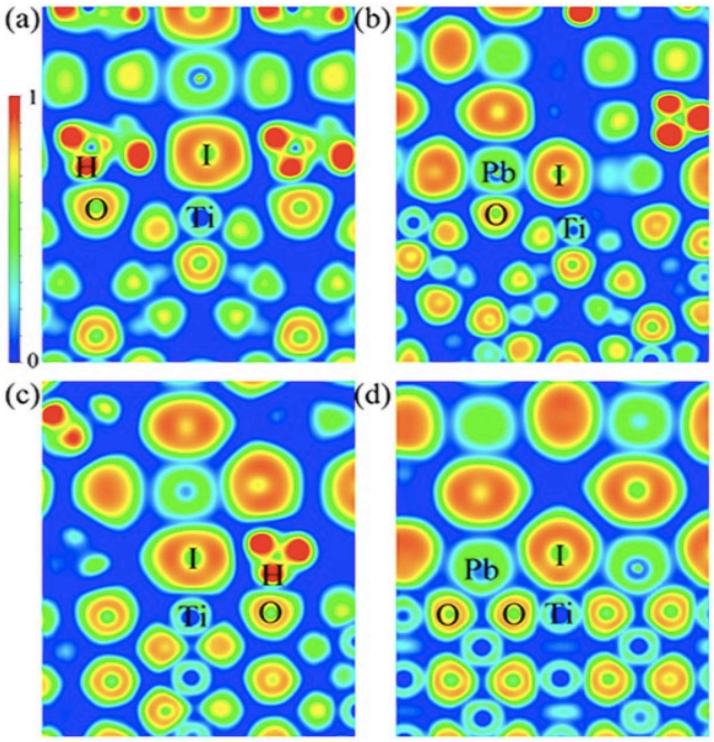

Figure 2.5 ELF plots at the interface (a) MAI/A (b) PbI/A (c) MAI/R (d) PbI/R [6]

Electron localization function (ELF) plots are useful in understanding the chemical interaction among the atoms. ELF plots range from 0 to 1, 0 represent no electron localization and 1 represents high electron localization, the value of 0.5 represents the electron gas like feature which is highly desirable as it supports the effective charge transfer across the interface. The respective ELF plots for each interface are shown in Fig. 2.6, it is seen that the electrons around H, I and O atoms are highly localized represented by red color, however, the electron clouds around the Pb and Ti has electron gas like attribute around them represented by green color. This indicates a better charge transfer attribute at PbI_2 terminated rutile TiO_2 interface, hence PbI_2 interface assists in more charge transfer.

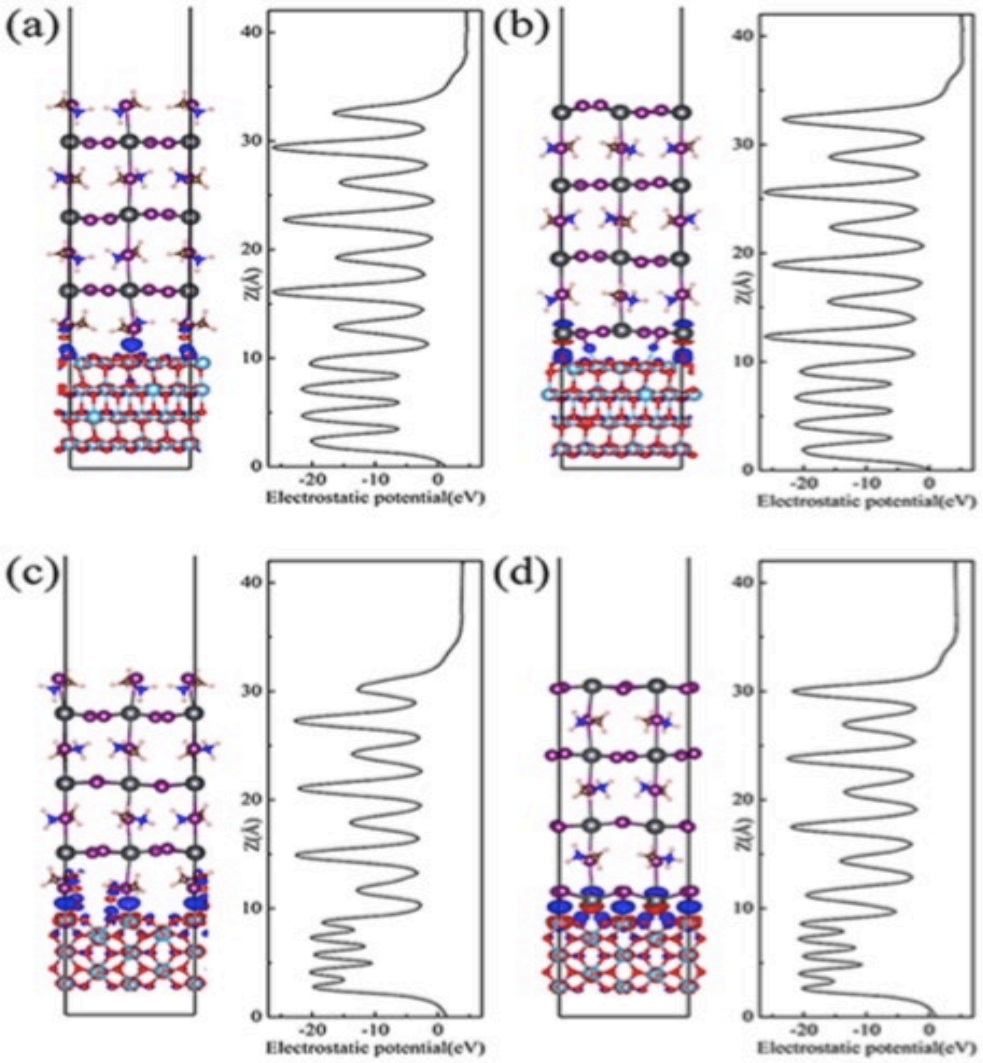

Figure 2.7 Electrostatic potential curves on the right and electronic charge density plots on the left side for perovskite/TiO_2 interfaces (a) MAI/A (b) PbI/A (c) MAI/R (d) PbI/R [6]

Electrostatic potential plots for the interfaces are shown in Fig. 2.7 (a) MAI/A (b) PbI/A (c) MAI/R (d) PbI/R. It can be concluded that the average electrostatic potential of TiO_2 is lower than the perovskite, which indicates the transfer of charge from perovskite to TiO_2 layer. Furthermore, the MAI layer is at higher potential compared to PbI layer thus the electrostatic potential drop at PbI terminated interface is deeper, which helps in accumulation of electrons at TiO_2 end, thus it will result in better charge separation at the

interface. Finally, the average electrostatic potential difference between perovskite and TiO_2 is higher in case of PbI terminated rutile TiO_2 (d) which will lead to better charge transfer across the interface compared to other cases.

Charge density plots shown in the left side of electrostatic potential plots can further explain electronic properties at these interfaces. Here, Blue and red colors represent charge accumulation and charge depletion respectively. It can be seen that, at the PbI terminated interface, the higher accumulation and depletion of charges occur between coordinated Pb and O atoms. This redistribution of the charges at the interface will result in electric dipole formation and lead to band bending to better support charge separation.

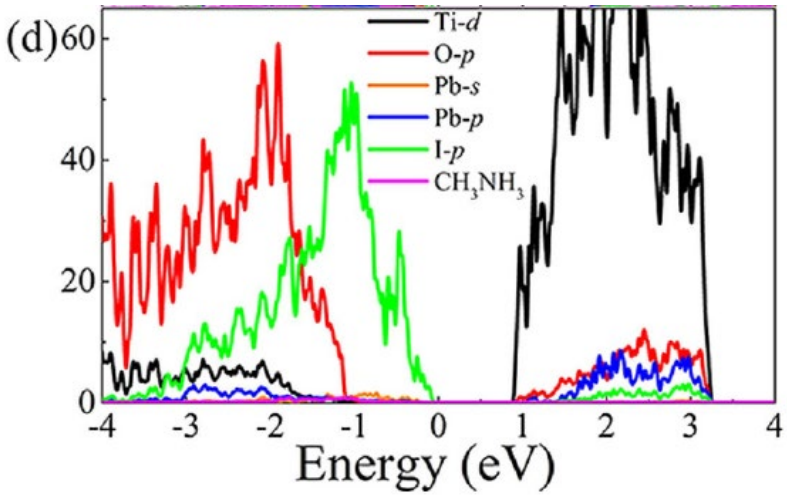

Figure 2.8 Projected DOS of different orbitals of perovskite with rutile TiO_2 interface [6]

Fig. 2.8 shows the PDOS (projected density of states) plots for perovskite adsorbed on rutile TiO_2 for PbI/R interface in order to understand the energy states available for charge transfer and electronic properties at the interface. Here, the bandgap of perovskite is relatively smaller compared to TiO_2 thus the electrons excite from valence band of perovskite (I-*p* and partly Pb-*s*) to conduction band of perovskite (Pb-*p* orbitals) and then those excited electrons are injected into the conduction band of TiO_2 (Ti-*d*). Therefore, the

photo-absorption efficiency depends on the gap between I-*p* and Pb-*p* and the electron injection efficiency depends on the gap between Ti-*d* and Pb-*p* [6].

2.5 Rutile and anatase TiO_2 for PSC application

Titanium dioxide is the most widely used metal oxide layer in PV cell technology as it acts as an electron transport material. Due to its high electron affinity, high stability, low cost and good surface matching with the perovskite material, it is most commonly used ETL layer in PSCs [15].

TiO_2 naturally occurs in rutile, anatase and brookite phases [11]. Both, anatase and rutile TiO_2 phases have been commonly used for PSCs applications. Anatase TiO_2 has certain drawbacks such as low electron mobility and lower charge separation compared to rutile phase. Whereas the rutile TiO_2 has better charge mobility and better charge separation, which make it more suitable to be used for solar cell applications and getting higher PCE [7].

The PCE of perovskite cells highly depends on the effectiveness of charge transfer taking place at perovskite/TiO_2 interface. Effective charge transfer and less charge recombination at the interface results in better overall cell efficiency.

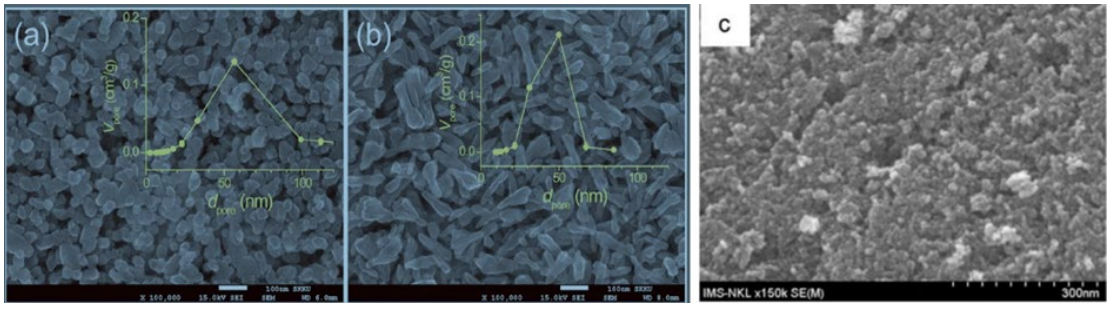

Figure 2.9 SEM image of (a) Anatase and (b) Rutile and (c) Brookite TiO_2 structures [8][9]

In order to compare the morphology of anatase, rutile and brookite phase, SEM images all three phases are presented in Fig. 2.9. Fig. 2.9 a) shows the morphology of hydrothermally synthesized anatase, and b) shows the rutile TiO_2 formed by hydrolysis of $TiCl_4$ and Fig. 2.9 (c) shows the hydrothermally synthesized brookite phase of TiO_2. It can be seen that the anatase and brookite TiO_2 has a spherical structure (a) and (c) whereas, the rutile TiO_2 has a long rod-like structure (b) [8]. The diameter of the anatase phase crystals is around 50 nm and the diameter of brookite crystals is around 10-12 nm, whereas the aspect ratio of the rutile phase is 0.2 (20 nm diameter and 100 nm long). Rutile and anatase phases of the TiO_2 are most commonly used for the solar cell application due to their better charge extraction and better surface contact with the active absorber layer. Due to their long rod-like structure, the rutile phase provides more surface area of contact at the adsorbing interface. Also, they have a slightly higher porosity compared to the anatase phase [8]. This geometry facilitates the formation of the smooth layer of perovskite on top of rutile TiO_2. Besides, the HTM and Au layers (as shown in Fig. 2.3 (b)) formed on rutile TiO_2 based perovskite cells are smooth as well, compared to anatase TiO_2 [8].

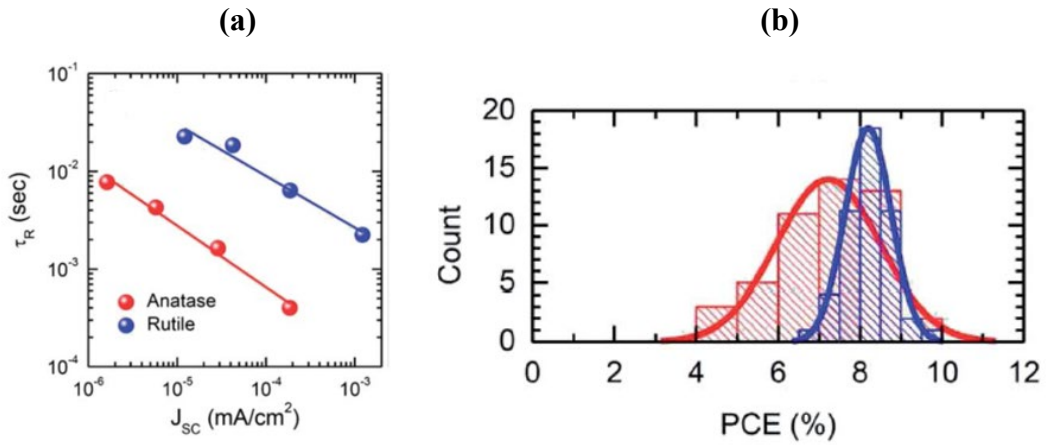

Figure 2.10 a) time constant for electron recombination (τ_R) versus short circuit current density, and b) the number of sample cells versus power conversion efficiency of anatase and rutile TiO_2 [8]

The time constant for electron recombination 'τ_R' values versus J_{sc} (short circuit current) are plotted and compared for rutile and anatase phases as shown in Fig. 2.9 a). It can be seen that the τ_R value for the rutile TiO_2 is ten times larger than that of anatase phase. Thus, the higher value of τ_R indicates the longer time required for recombination of separated charges which means a higher number of electrons injection into rutile TiO_2 and better charge separation [8] [10].

The PCE of 48 device samples of anatase and rutile-based perovskite solar cells are compared and the results are plotted in the histogram shown in Fig. 2.9 b). The rutile-based cells show less standard deviation in PCE; hence they are more consistent to reproduce [8]. Based on the comparison, it can be concluded that the rutile TiO_2 based perovskite cells have better charge transfer, lesser recombination losses, higher reproducibility and better interfacial contacts with the perovskite material.

2.6 The (001) surface of TiO_2

2x2x3 arrangement of the unit cell structure of rutile TiO_2 best matches with the lateral dimensions of the perovskite crystal. However, two possible planes can be selected for the simulation. The (001) plane which has a lateral area of 9.174 x 9.174 $Å^2$ and the (100) plane with 8.877 x 9.174 $Å^2$. Although the (100) plane has a better match with the perovskite surface area wise, here we have selected the (001) plane of TiO_2 and the reasons are justified in the following paragraphs.

The electric conductivity of the TiO_2 is higher along the (001) plane which is highly desirable for cell performance. Better conductivity enhances effective charge transfer across the solar cell [11].

Labat et al. [13] investigated different planes of TiO_2 phases to compare the surface energy of various planes using different computational functional. The calculated surface energies of the surfaces are given in the following order: (101) anatase < (110) rutile < (100) anatase < (100) rutile << (001) rutile. The rutile (001) surface has the highest surface energy compared to other surfaces, which makes it a more reactive surface. The high reactivity of the (001) plane helps in better attachment of TiO_2 with perovskite surface compared to the (100) plane [12].

Huang et al. compared the 2 planes of the anatase TiO_2, (001) and (101). The results show that (001) plane of anatase TiO_2 has high reactivity compared to the (101) face, which makes it more suitable for the perovskite solar cell applications. it supports electron extraction in the cell interface and reduces charge carrier loss in ETL [13].

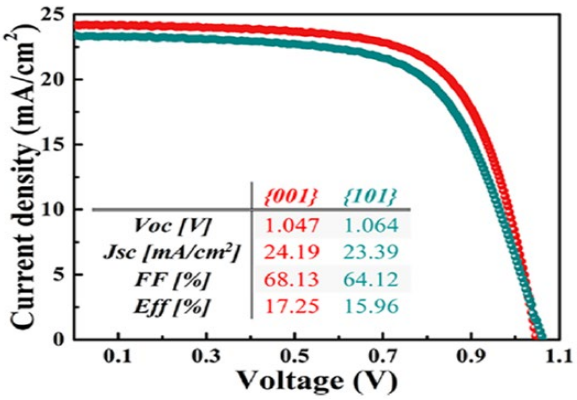

Figure 2.11 J -V characteristics of perovskite solar cell for anatase (001) and (101) planes [13]

The short circuit current density, open-circuit voltage, fill factor and overall efficiency is calculated as shown in Fig. 2.11. The current densities for (001) and (101) plane of anatase TiO_2 are plotted with respect to the voltage generated to compare the cell

performance. The overall power conversion efficiency obtained for the (001) plane is 17.25%, which is better than that of 15.96 % of the (101) plane [13].

The requirements for the ideal ETL are closely fulfilled by (001) facet, which are: 1) (001) facet has better transparency than (101) facet, high transparency results in a lower loss of incident light. 2) (001) plane has less surface roughness, smoother surface results in better electric contact and reduces interface resistance. 3) (001) facet shows better electron extraction ability due to the smoother surface and provides better wettability which reduces charge recombination. 4) 'I-V' plot of (001) vs (101) plane shows better conductivity of the (001) facet compared to the (101) facet, which reduces the carrier transport losses at the interface. The reasons for the better conductivity are referred to as the abundance of Ti^{3+} ions in the (001) facet and better morphology of the plane [13].

2.7 Interfacial modifiers for surface passivation

To improve cell performance, it is essential to understand electronic properties and charge transfer mechanism taking place at various interfaces of the solar cell. One of the factors limiting the performance of PSCs is the formation of trap states at these interfaces. It has been seen that the formation of trap states at perovskite/TiO_2 interface causes recombination of separated charges between ETL and HTM which will compromise the overall power conversion efficiency. These trap states are formed due to the accumulation of charge carriers at the interface. Passivation of these trap states can reduce the recombination of charges in perovskite solar cell to improve overall efficiency [16] [17].

There are several methods for reducing these recombination losses. One of the proven methods is the introduction of a thin film of the passivation layer between the

perovskite/TiO_2 interfaces. This method has been successfully used by various researchers [20] [23].

Modifying the perovskite/TiO_2 interface with 4 –Mercaptobenzoic acid (MBA) improves charge transfer by surface passivation or inhibiting trap states as it acts as an anchoring molecule to adsorb perovskite on TiO_2 that helps in effective electron injection [16].

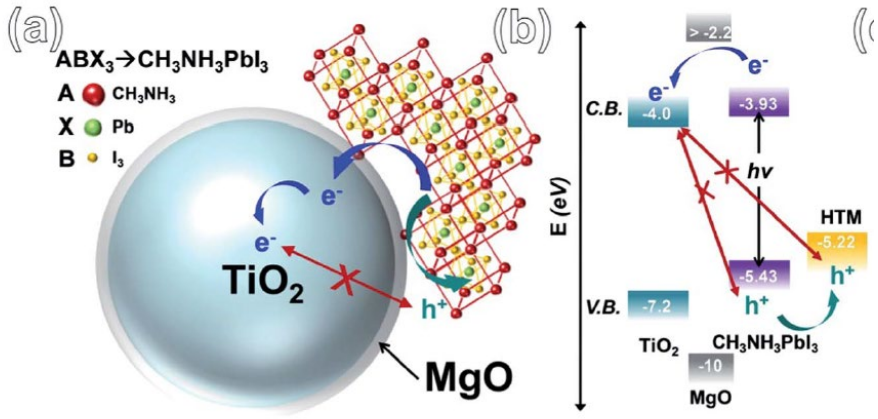

Figure 2.12 Interface modification of PSC with MgO a) interface b) band structure [18]

Fig. 2.12 (b) shows the band structure of the perovskite/TiO_2 interface incorporated with a magnesium oxide (MgO) layer. The thin layer of large bandgap MgO prevents the recombination of the separated charge by blocking the reverse charge transfer [18]. MgO molecule acts as a hole blocking layer hence preventing recombination losses and improving electron injection at the interface. Also, a spike in energy bands at perovskite/TiO_2 interface can enhance the power conversion efficiency [19]. When MBA molecule is connected to TiO_2, direct electron transfer takes place through tunneling in case of Ag nanoparticle-based solar cells [21].

The same transfer of electron at the perovskite/MBA/TiO_2 could be the reason for improved charge transfer. To reduce the recombination losses, a positive band offset at the absorber/ETL interface has been shown to improve the cell performance [22].

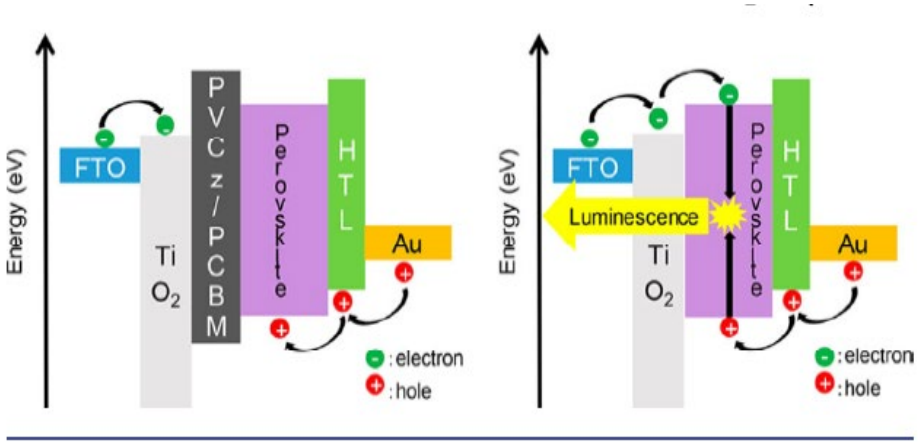

Figure 2.13 Interface band gap representation of modified PSCs [24]

Incorporating the Poly (vinyl carbazole) PVCz and PCBM layer between the perovskite/TiO_2 interface helps in surface passivation. Band energy diagram of interface modified perovskite cell with and without PVCz/PCBM layer is shown in Fig. 2.13. The inserted layer has deep HOMO (-6.0 eV) and shallow LUMO (-2.3 eV) levels compared to those of the perovskite layer. This large bandgap layer is responsible for the prevention of the recombination and increasing overall charge transfer in the cell [24].

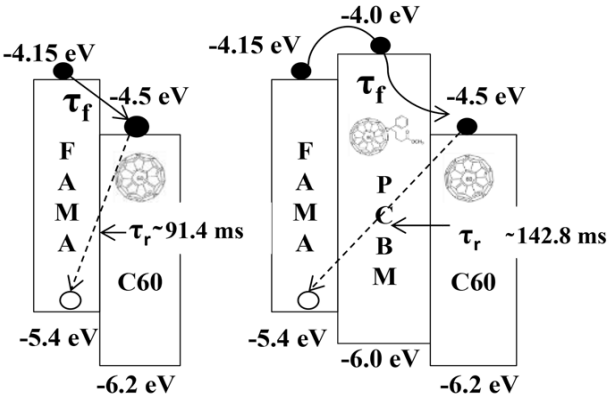

Figure 2.14 charge extraction and recombination process [25]

Fig. 2.14 represents the energy level alignment of a solar cell made of FAMA perovskite material and C_{60} used as ETL. The layer of PCBM placed between the absorber/ETL interfaces improves the FF (fill factor) which is responsible for improving PCE. Introduction of molecule results in spike band structure at the interface which is responsible for the surface passivation and suppression of the recombination. The layer prevents the recombination of separated charge as more activation energy is required for the electrons to cross the layer acting as a barrier [25].

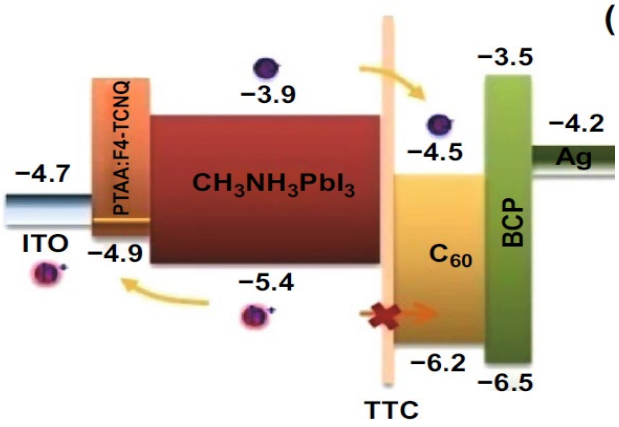

Figure 2.15 Energy band level diagram of interface modified perovskite solar cell [26]

Fig. 2.15 shows the energy band levels of one of the hybrid perovskite/C_{60} modified cells with tetratetracontane (TTC) as an interfacial layer. Here the TTC layer acts as a

passivation layer as well as hydrophobic water-resistant layer. In this case, the transfer of electrons from the absorber layer to C_{60} takes place through tunneling as there are energy matching states available to tunnel through. Additionally, there are no energy matching unoccupied states available for tunneling of holes, which prevents the recombination losses, hence the layer allows the transfer of electrons effectively and blocks the transfer of holes at the interface [26].

2.8 Thiols as interfacial modifiers

As we discussed earlier, perovskite cells have poor stability in environmental conditions as they easily degrade in the presence of oxygen, moisture and heat. Also, they suffer from recombination losses due to generation of trap states at the HTL/absorber/ETL interface. One of the approaches to solve these issues is by modifying the HTL/perovskite/TiO_2 interface with a thin organic monolayer which has proven to improve the cell performance and stability [14].

It has been seen that the incorporation of carboxyl acid-thiol (HOOC-Ph-SH) between $CH_3NH_3PbI_3/TiO_2$ improves cell efficiency by enhancing charge transfer at the interface [14] [16]. Additionally, a hydrophobic thiol layer of HS-C_6F_5 placed at $CH_3NH_3PbI_3$/HTM interface helps improve stability by inhibiting water intrusion in the cell interface [15].

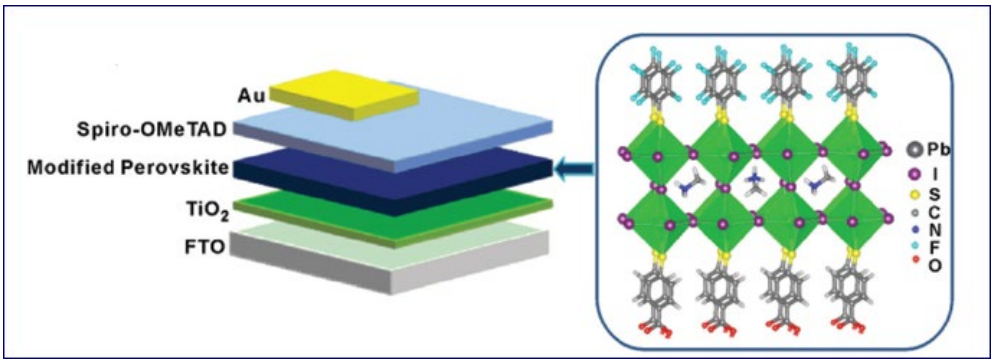

Figure 2.16 Modified perovskite cell interface with thiol monolayers [14]

Fig. 2.16 shows the cell architecture of modified interfaces of hybrid PSC. 4-mercaptobenzoic acid (HOOC-Ph-SH) is deposited onto the TiO_2 before deposition of perovskite. The perovskite is then covered with pentafluoro-benzenethiol ($HS-C_6F_5$) layer in order to prevent intrusion of water inside the cell.

(a) **(b)**

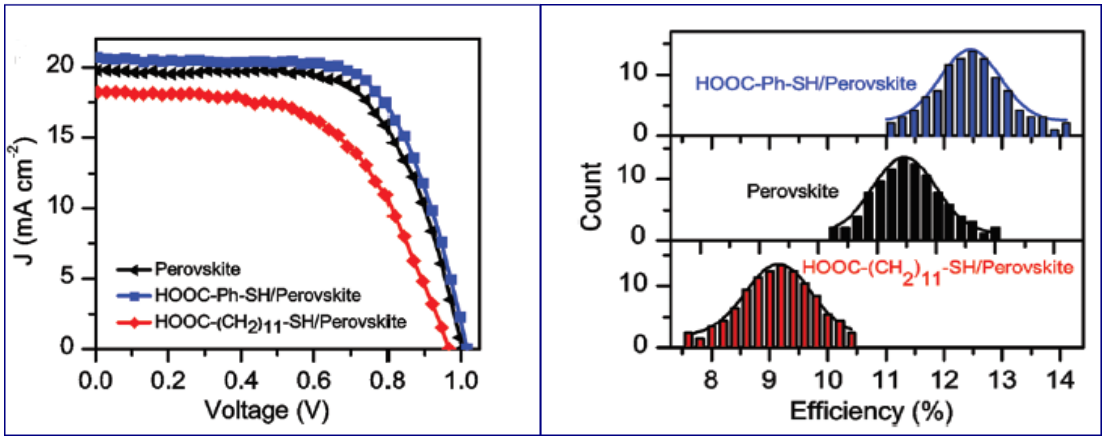

Figure 2.17 (a) J-V characteristics and (b) number of samples versus % efficiency plot of the modified cell [14]

The performance of the interface-modified hybrid perovskite is compared with perovskite solar cell without modification. Fig. 2.17(a) and (b) show the J-V characteristics and % efficiency for tested samples. Overall performance of the hybrid PSC cell with thiol (HOOC-Ph-SH) incorporation of 100 fabricated samples was tested and the average

efficiency of 12.4 ± 1.8 % is observed compared to perovskite without the MBA layer for which 11.6 ± 1.6 % efficiency is obtained [14].

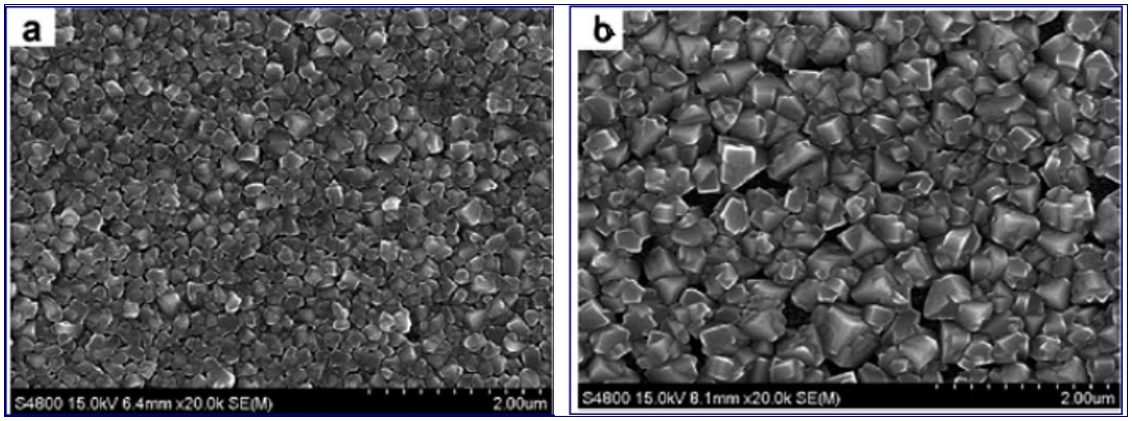

Figure 2.18 SEM showing a) perovskite/TiO_2 b) TiO_2/HOOC-Ph-SH/perovskite deposited on FTO [14]

The improved performance is considered due to better charge transfer caused by π-electron transfer method, which also slows down the recombination losses at the interface. Additionally, the perovskite layer formed onto the HOOC-Ph-SH layer improves the overall solar cell morphology by forming larger crystals of perovskite onto the thiol layer as compared to the perovskite only film. This difference can be visualized in SEM images of the crystal structure of perovskite with and without MBA layer compared in Fig. 2.18 a) and b).

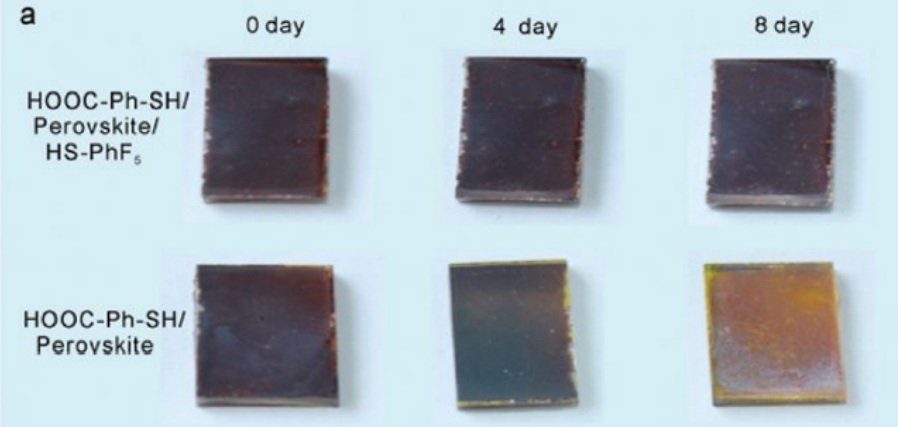

Figure 2.19 The color variation of the perovskite cell covered with and without HS-PhF_5 layer placed in the air with 45% humidity [14]

When water meets $CH_3NH_3PbI_3$, it removes the organic methylammonium molecule and breaks down the perovskite material. Covering the perovskite structure with the hydrophobic thiol (HS-C_6F_5) layer has shown to protect perovskite from degradation due to moisture and improve the stability of the overall cell. The cell with an added layer of thiol (HS-C_6F_5) onto perovskite material seems to keep 80% of its prior efficiency after 10 days period, whereas cells without thiol layer lost about 80% of its original efficiency in 10 days. Fig. 2.19 shows discoloration of the cell without thiol layer, it turns yellow after 8 days, whereas the cell with hydrophobic layer retains its color even after 8 days, which is the indication of improved stability of the cell [14].

CHAPTER 3 METHODOLOGY

In this section, we will discuss the theory for simulations and also explain the software used and parameters considered. In this work, we use a computational materials science approach for structural optimization and calculation of electronic properties. It represents running the experiments on the computer in order to obtain and interpret the results without actual physical experiments. This can save a large amount of time and efforts. The advantages of the computational methods are its versatility, accuracy and low cost. We can easily modify the structures and set constraints on atoms to focus on the specific locations to analyze the behavior of the system.

Here we use VASP (Vienna ab initio simulation package) to run density functional theory (DFT) calculations [27-30]. DFT states that the ground state energy of a system can be approximated by electron density distribution, which can be used to measure various electronic properties of the system. 'Ab initio' means from the beginning, as it uses the quantum mechanical approach from the first principle wave basis set for calculating the ground state of electrons. This method has shown to provide the most reliable and accurate results for ground-state energy calculations.

3.1 Introduction to density functional theory

DFT is a quantum mechanical method used for computing structure and electronic properties of atoms and molecules. DFT uses electron density of atoms to analyze various properties of the material. As most properties of a material depend upon the valence

electrons present in the outer shell of the atom, thus DFT focuses on outer shell electrons. DFT uses various functionals to define the inner and outer electron density [31].

In quantum mechanics, the particle is defined by its wave function. The Schrödinger equation is a partial differential equation which is used to find the wave function of a particle at any time when we know the wave function of the particle at t=0. Thus, the ground state energy of a system can be found by solving the time-independent Schrödinger equation. It is easy to solve the Schrödinger equation for a single body system such as hydrogen atom which has a single electron, however, it becomes impossible to solve the Schrödinger equation for many-electron system. DFT comes into consideration to make this simple by considering various functionals to solve the many-body Schrödinger equation [31].

Hohenberg and Kohn published a paper in 1964, which provides the foundation for the DFT. Many-body wave-function depends on 3N variables, where N is the number of electrons, whereas the electron density can be defined by only 3 spatial coordinates X, Y and Z in space [32].

Two theorems are stated by Hohenberg and Kohn for explaining DFT, the first theorem states that the ground state energy of a system is unique functional of the electron density. Thus, the electron density functional is directly related to the system properties. In other words, ground-state electron density can be used to determine all the quantum properties including the ground state energy and wave function of the ground state.

Time independent Schrödinger equation is given by

$$H\Psi = E\Psi \tag{3.1.1}$$

Here, *H* is the Hamiltonian operator, Ψ is the wave function of the system and *E* stands for eigenvalue energy of stationary state Ψ. The Hamiltonian operator can be expanded as follows,

$$H = \frac{-\hbar^2}{2m}\sum_{i=1}^{N}\nabla_i^2 + \sum_{i=1}^{N}V(r_i) + \sum_{i=1}^{N}\sum_{j<i}U(r_i r_j) \tag{3.1.2}$$

In the equation 3.1.2, m is mass of an electron, the first term includes the total kinetic energy of all electrons, the second term is potential energy due to Coulomb interaction of nuclei with electrons and the third term defines the electron-electron interaction energy.

In the above equation, *V(r)* is the external potential which is responsible for the interaction of electrons with atomic nuclei. Electronic density $n(r)$ at the ground-state Ψ is a function of external potential $V(r)$ as the wave function $\psi(r)$ can be decided by $V(r)$,

$$n(r) = \int \prod_{i=2}^{N} dr_i |\Psi(r, r_2, \dots, r_N)|^2 \tag{3.1.3}$$

Here, the ground-state electron density $n(r)$ can affect the external potential $V(r)$ and thus the Hamiltonian operator and hence all the ground state properties of the system can be found. As $n(r)$ and $V(r)$ are inter-dependent, they should be found self-consistently.

The second theorem states that the energy functional attains minimum only at the true ground-state electron density. Thus, electron density that minimizes the overall energy functional of the system is the true ground state density.

$$E[n(r)] > E_0[n_0(r)] \tag{3.1.4}$$

The energy functional term can be separated into two main parts one of which is known and the other one is unknown.

$$E[\{\psi_i\}] = E_{known}[\{\psi_i\}] + E_{xc}[\{\psi_i\}] \tag{3.1.5}$$

Here, known term consists of four terms, the kinetic energy of the electron, electron-nuclei coulomb interaction, electron-electron Coulomb interaction and Coulomb interaction between nuclei. The unknown term is the exchange-correlation term, which includes purely quantum mechanical effects, and needs to be approximated.

In order to find the ground state energy of the system from electron density, we need to define exchange-correlation functional. We know that exchange-correlation functional exits but unfortunately, we don't know the exact exchange-correlation functional, therefore various approximations have been developed in order to get the results. One of the simplest exchange-correlation functional is local density approximation (LDA). In LDA, the local electron density is assumed to be that of a homogeneous electron gas which is considered to define the approximate exchange-correlation functional. In the case of generalized gradient approximation (GGA), both local electron density and its gradient are considered for approximation. Continuous researches are going on in order to improve this exchange-correlation functional to obtain accurate results.

To use density functional theory practically, Kohn and Sham provided a set of equations to solve the Schrödinger equation in order to obtain the ground-state electron density in which each equation involves only one electron. Kohn Sham scheme is given in the form,

$$\left[\frac{-\hbar^2}{2m}\nabla^2 + V(r) + V_H(r) + V_{xc}(r)\right]\psi_i(r) = \varepsilon_i\psi_i(r) \qquad (3.1.6)$$

The terms in the equation 3.1.6 are defined as, the kinetic energy of an electron, external potential *V(r)* among the electron and nuclei, Hartree potential (V_H) which includes the coulomb self-interaction of an electron with electron density. Here, V_{xc} is the exchange-correlation potential, which needs to be approximated by exchange-correlation functional.

DFT uses a self-consistent scheme to solve a set of Kohn sham equations. It involves first guessing some approximate electron density (trial n(r)), which is used to solve the Kohn sham set of equations in order to obtain single electron wave function $\psi_i(r)$. From obtained single electron wave function, it recalculates the electron density which is called as calculated n(r). When the calculated electron density is close enough to the trial electron density, we find self-consistency in our loop and we obtain the ground state density. After calculating the ground-state electron density, all the structural and electronic properties of the system can be calculated [31].

3.2 Introduction to VASP

In this research, all the electronic calculations are performed using VASP, which stands for 'Vienna ab initio simulation package'. It is one of the most accurate tools widely used for performing DFT calculations. 'Ab initio' is a Latin term which can be translated as 'from the beginning', as all the calculations in VASP are performed using first-principles. Pseudopotentials and projector augmented wave (PAW) method and plane-wave basis set are used in VASP to include electron-ion interaction. It applies periodic boundary conditions in three spatial planes. It can model the system with a maximum of hundreds of atoms [35].

Most of the names of input and output files of the VASP ends with CAR and it stands for 'card'. The main input files for running calculations in VASP are as follows.

- INCAR: This is the main input file required for running the calculations in VASP. It consists of several tags associated with different parameters which tell VASP to

run the calculations accordingly. Some of the tags define geometric and ionic relaxation parameters, energy cutoffs, global break conditions, number of electronic and ionic steps etc.

- POSCAR: It consists of geometric cell parameters of the unit cell, the lattice constant, number of atoms of each species with coordinates of each atom and constraints (if any) on them. The type of co-ordinates whether direct or Cartesian is also mentioned in this one. The order of the lines is very important in this case as any inconsistency will result in error hence stopping the calculation immediately.
- POTCAR: This file consists of the pseudopotentials of all the species taking part in the calculation and the same order of types of atoms should be used in the POSCAR file while assigning the co-ordinates. VASP database provides the files for each of the species which can be combined for multiple species system. It also contains primary information about atoms such as mass and valency.
- KPOINTS: It contains information about k-point mesh size in order to define the repetitive cell structures.

Based on the input parameters assigned in the INCAR file, a number of output files are generated. Some of the major output files of VASP are as follows.

- OUTCAR: It is the most important output file of the simulation. It contains all the information about input files and resulting calculations such as the position of atoms, forces acting on them, eigenvalues of the system, total computing time, the total energy after each ionic step etc.

- CONTCAR: it contains resulting coordinates of the optimized atoms after completing the calculations. It has the same format as that of POSCAR so it is usually used further for continuing the calculations.
- CHGCAR: it contains information about the charge density of the system with atomic coordinates and lattice vectors. It is usually a very big file used for visualization. The CHG file is used to find the charge density of the included atoms.
- OSZICAR: it contains information about ionic and electronic steps such as their convergence speed and energy after each step.

3.3 Calculation settings for VASP

For running the calculations in VASP we need to specify the input parameters in various input files mentioned above. In order to accurately analyze the interaction among non-bonded atoms, we have included the van der Waals interactions among the atoms for calculations. The k-point mesh size used is 3x3x1 for TiO_2 for surface reconstruction and 1 gamma point for a monolayer. Plane-wave cutoff energy for basis function is set to 600 eV, 1000 number of ionic steps are set, the maximum force on each atom after optimization is set to 0.01 eV/A, IBRION value is set as 2 for ionic relaxation. 'Perdew-Burke-Ernzerhof revised for solids' exchange-correlation functional is used. Also, the symmetry is switched off for all the calculations.

CHAPTER 4 RESULTS AND DISCUSSION

The current simulation study aims at investigating the effects of 4- mercaptobenzoic acid monolayer adsorbed on TiO_2 surface in order to analyze the structural and electronic properties such that it will help us understand the improved performance in hybrid perovskite solar cells. This section consists of a detailed procedure for atomic optimization and explanation for results of optimization for various interfaces between TiO_2 and HOOC-Ph-SH (4-mercaptobenzoic acid) monolayer. For the visualization of the optimized TiO_2 and HOOC-Ph-SH, we use a visualization software named VESTA (Visualization for Electronic and Structural Analysis). We have obtained the coordinates of TiO_2 from the literature [11]. We use VASP (Vienna ab initio simulation package) for the structural optimization of all the structures.

We first create the bulk structure of TiO_2 using VESTA with the obtained coordinates and optimize it using VASP. This resulting optimized bulk structure of TiO_2 is further used to construct a 2x2x3 structure of TiO_2 slab for (001) surface reconstruction. For surface reconstruction, we use selective dynamics approach in which the bottom layers of the structure are constrained and top layers are allowed to relax. A vacuum of 30 Å is added to the structure for the surface reconstruction to avoid the distortion of the surface due to interaction of periodic arrangement of atoms.

A total number of nine potential sites are selected to place the molecule onto the TiO_2 structure such as to cover the maximum possibilities of the molecule attachment onto the TiO_2 surface. After the optimization of these nine interfaces, we selected two of the most stable structures with the lowest total energy and further analyzed them for studying

the electronic properties. We analyzed the electrostatic potential, charge density, electron localization function, charge density difference, the density of states and partial density of states of the most stable structures in order to understand the interaction of the molecule with the TiO_2 interface.

4.1 Unit cell optimization and surface reconstruction of Rutile TiO_2 surface

The first step of the calculation is the optimization of the unit cell of rutile TiO_2. We have considered the rutile phase of TiO_2 for our calculations through literature review. We have already discussed the benefits of using rutile TiO_2 for perovskite solar cell applications over an anatase phase in the literature review part. The unit cell of rutile TiO_2 has a tetragonal structure at room temperature. We use the unit cell co-ordinates from the literature [15] to create the structure using VESTA software.

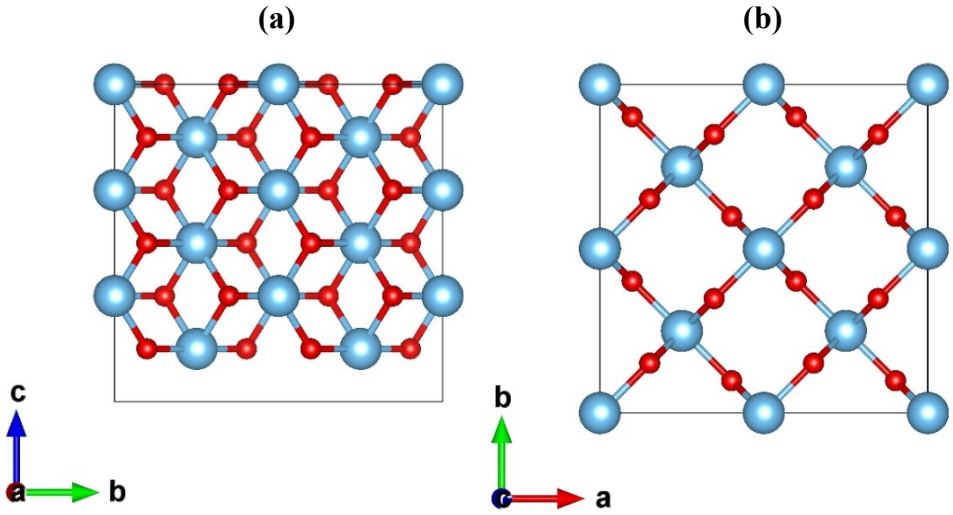

Figure 4.1 a) side view and b) top view of bulk TiO_2 structure

We optimized the bulk TiO_2 unit cell (Ti_2O_4) in VASP using input parameters such as k-point mesh 6x6x6, plane wave cut off: 600 eV and maximum force on each atom after

optimization: 0.01eV/ Å. The resulting optimized bulk TiO_2 unit cell is used to make the 2x2x3 structure of TiO_2 slab using VESTA which will be further optimized for surface reconstruction. The 2x2x3 cell geometry is selected for surface reconstruction of TiO_2 such that the lateral dimensions of the structure have good lattice matching with that of perovskite structure on the (001) plane. Fig. 4.1 a) and b) show the side view and the top view of the created TiO_2 bulk unit cell respectively. The unit cell structure consists of 6 layers of titanium and oxygen with a total of 72 atoms. The slab dimensions are 9.174 Å x 9.174 Å x 8.877 Å with total slab volume obtained is 707.108 $Å^3$.

Surface reconstruction allows the atoms at the surface to relax and act similar to the realistic interface as compared to the bulk atoms. For the surface reconstruction optimization, we use a 6-layer slab structure of TiO_2 as shown in Fig. 4.1 a), the bottom 3 layers are kept fixed using selective dynamics and the top 3 layers are free to relax. Also, a vacuum of 30 Å is added to the slab in Z-direction in order to avoid distortion of the atoms due to periodic repetition. Therefore, the total length of the unit cell obtained along c-direction is 38.877 Å.

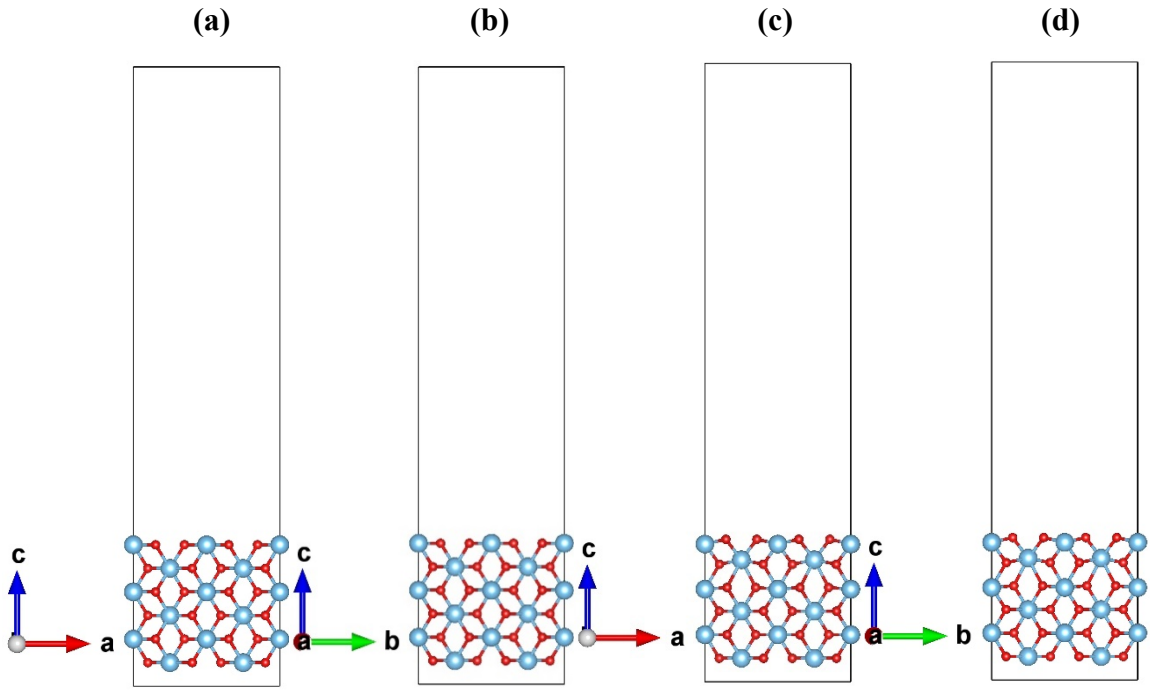

Figure 4.2 a) and b) show two views of TiO_2 structure before surface reconstruction with 90 rotations between them and c) and d) shows the two views of the surface reconstructed TiO_2

Fig. 4.2 a) and b) shows two views of TiO_2 rotated 90 degrees sidewise before the surface reconstruction and c) and d) shows the surface reconstructed structure rotated 90 degrees sidewise, with an added vacuum of 30 Å. When we observe surface reconstructed structure, we can see the relaxation of the upper layer of oxygen and titanium atoms that slightly moved upwards in the Z-direction.

The angle between the Ti-O-Ti bond is changed from 130.77 degrees to 127.60 degrees. When we compare the top 3 relaxed layers with the bottom 3 fixed layers, we can see the relaxation of the non constrained atoms. The top 3 layers are gradually expanded upwards. The verticle distance between the Ti-Ti atoms which are right on top of each other is increased by 0.272 Å and verticle distance between the oxygen atoms is increased by 0.077 Å.

4.2 Optimization of 4-mercaptobenzoic acid(HOOC-Ph-SH) monolayer

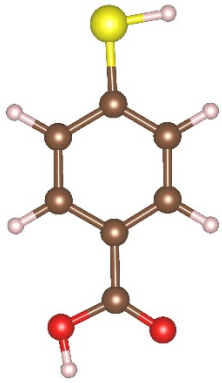

Figure 4.3 HOOC-Ph-SH (4-mercaptobenzoic acid)

The next step is to optimize the 4-mercaptobenzoic acid molecule which will be used for the interface formation [39]. It has been experimentally proven that the MBA monolayer HOOC-Ph-SH placed between the TiO_2/$MAPbI_3$ acts as an anchoring molecule to the interface and helps improve the charge transfer across the cell [14]. We use VESTA and Gausview to create the structure of 4-mercaptobenzoic acid which has the chemical formula of HOOC-Ph-SH. Fig. 4.3 shows the structure of the molecule with 16 atoms. It is also known by several other names such as 4-sulfanylbenzoic acid, 4-mercaptobenzoate etc. For optimization, we use 20x20x20 $Å^3$ unit cell dimensions. We use the same settings for VASP as that used for TiO_2, except the value for k-points is set equal to 1 (gamma point), as the molecule does not need periodic structure.

4.3 Optimization of TiO_2/4-mercaptobenzoic acid interfaces

After the surface reconstruction of TiO_2 and optimization of the molecule from monolayer, we have selected three different atomic arrangements of the monolayer to place

at three different sites on the TiO_2 (001) surface. Which gives us a total of nine interface combinations for the optimization of the TiO_2/monolayer interface. We tried to keep the monolayer as straight as possible at respective sites. For interface optimization also we constrained the bottom three layers of TiO_2 and the rest of TiO_2 and entire monolayer are free to relax. The total volume of the slab is kept the same as that of surface reconstructed TiO_2 and the total lateral height of the slab obtained is 38.877 Å.

As the experimental results from the study of Cao et al. [14] shown that the attachment of the molecule onto the TiO_2 takes place from the O-OH end, we choose this particular end to create all the interfaces. We selected 3 different sites on the (001) plane of TiO_2 surface for monolayer placement.

The first placement of monolayer is on top of the two oxygen atoms such that the distance of the specific atom of monolayer remains the same from both the oxygen atoms. The second placement is on top of the two Ti atoms such that the distance of the specific atom of monolayer remains the same from both of the Ti atoms. And the third placement is vertically right on top of the center Ti atom. The atomic sites of the molecules selected are carbon end, OH end and oxygen end. The resulting interfaces we get are a) carbon between two oxygens, b) carbon between two Ti, c) carbon on top of a centre Ti, d) OH between two oxygens, e) OH between two Ti, f) OH on top of a center Ti, g) O between two oxygens, h) O between two Ti, i) O on top of a center Ti.

The initial distance between the atoms is set by adding 1.5 Å, that is almost half of the Van der Waals separation to the respective bond length. This allows the possibilities of both physisorption and chemisorption to be determined by the optimization. For calculating bond length we used Gaussview software and verified the results with the published

literature [36]. The bond length between the O-O atoms is 1.2 Å, we have added extra 1.5 Å and kept the total distance 2.72 Å between them. For the T-O atoms the bond length is 1.98 Å, we added 1.5 Å and kept the total distance of 3.48 Å between Ti and O atoms. The placement of the molecule on top of TiO_2 is such that the initial distance between the Ti and O is approximately 3.48 Å and the initial distance between O-O atoms is approximately 1.72 Å.

For optimization, we use the same settings for running VASP calculations as that of TiO_2 surface reconstruction. All the nine initial interfaces formed are shown in the Fig.s 4.4 a), b), c), d), e), f), g), h), i) respectively.

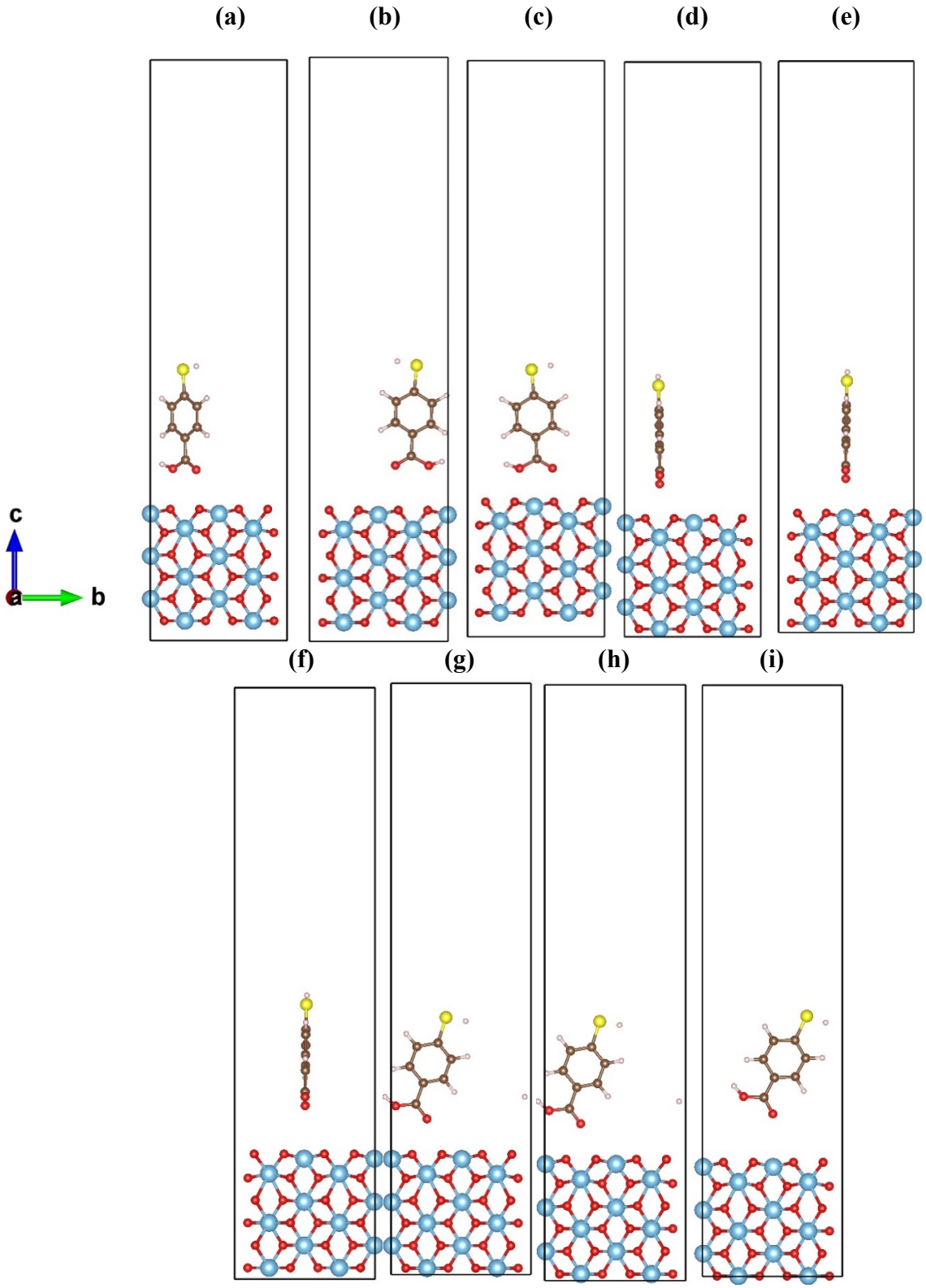

Figure 4.4 Surface reconstructed TiO_2 structures with the monolayer HOOC-Ph-SH placed at 9 different initial locations from a) to i).

4.4 Results for the optimization at the TiO_2/HOOC-Ph-SH interfaces

The results of the optimization of TiO_2/HOOC-Ph-SH interfaces are depicted in Fig. 4.5 (a, b, c, d, e, f, g, h, i). We can see in all the cases, there is a chemical bond formation between the 4-mercaptobenzoic acid and TiO_2 at the interface. For the first two carbon sites, the monolayer is displaced from its original placement and attached to two titanium atoms forming two Ti-O bonds as shown in Fig.4.5 a) and b). For the 3rd carbon site, two of the oxygen atoms of the monolayer are attached to the same central titanium atom forming O-Ti-O bond shown in Fig. 4.5 c). For the OH sites, the OH end placed between the two oxygen atoms is displaced and attached to the Ti atom forming a Ti-O bond with the OH end as shown in Fig. 4.5 d). For the OH site placed in between two Ti atoms of TiO_2, the monolayer is displaced and attached to the center Ti atom forming O-Ti-O bond shown in Fig. 4.5 e). The OH site placed on top of the central Ti atom, attached to the Ti atom forming Ti-O bond with the same end shown in Fig. 4.5 f). For the first two oxygen sites the monolayer is displaced from its original placement and attached to two titanium atoms forming Ti-O bonds as shown in Fig. 4.5 g) and h). For the oxygen end site placed vertically on top of the center Ti atom, the monolayer attached to the Ti atom forming two Ti-O bonds with the same Ti atom shown in Fig. 4.5 i).

In all the resulting cases, there is a chemical bond formation between Ti and O atoms with the bond length of approximately 2.06 Å. The presence of chemical bond formation at the interface enhances the charge transfer through the molecule and also provides flexibility to the overall cell structure. Also, it has been seen that the presence of

HOOC-Ph-SH at the interface will help in the formation of large crystals of perovskite deposited, which will again help in improving cell performance [14].

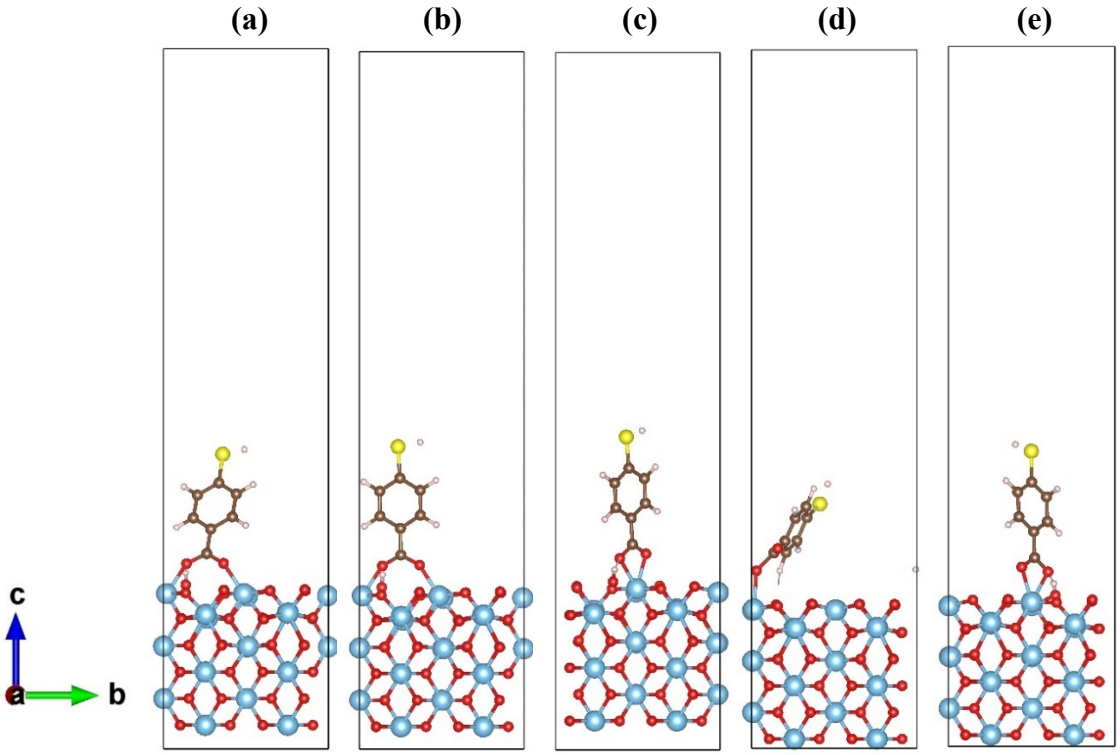

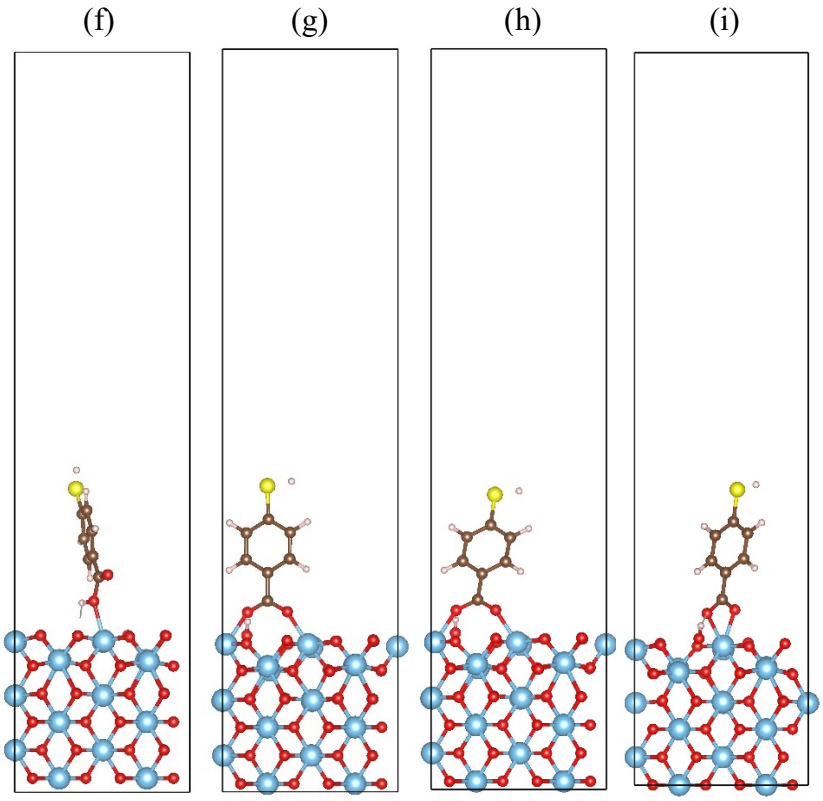

Figure 4.5 TiO_2/HOOC-Ph-SH interfaces after optimization from a) to i)

The total energy of all the optimized interfaces is extracted and tabulated in table 1. The total energies are important in analyzing the stability of the interfaces. Two of the most stable interfaces based on lowest total energies are 'carbon atom of the molecule placed between Ti atoms' and 'oxygen atom of the molecule placed between oxygen atoms of TiO_2' selected for analyzing the electronic properties further. The presence of the chemical bond between the molecule and TiO_2 enhances the charge transfer at the interface due to π-electron bond formation which is supported by Cao et al. in the literature [14].

Interface type (TiO_2/HOOC-Ph-SH)	Total energy (eV)	Selection
Carbon-between-O	0.020	
Carbon-between-Ti	0	Most stable
Carbon-on-top-Ti	0.295	
OH-between-O	1.538	
OH-between-Ti	0.295	
OH-on-top-Ti	1.751	
Oxygen-between-O	0.003	Second most stable
Oxygen-between-Ti	0.019	
Oxygen-on-top-Ti	0.303	

Table 1 Interface type and total energies of the optimized HOOC-Ph-SH interfaces with HOOC-Ph-SH monolayer.

4.5 Electrostatic potential

In order to understand the charge transfer mechanism at the interface, electrostatic potential plots are analyzed for two of the most stable interfaces and the results are compared with the published pieces of literature. For calculation of the electrostatic potential curves, we use P4VASP software and plotted the result using Gnuplot. The LOCPOT file from the VASP output which holds all the required information for the electrostatic potential is used for plotting the electrostatic potential curves.

Fig. 4.6 shows the minimum, average and maximum electrostatic potential plots of optimized surface reconstructed TiO_2 and the magnified average electrostatic potential of TiO_2 is further depicted in Fig. 4.7. Fig. 4.8 and 4.10 show the minimum, average and maximum electrostatic potential versus distance in Å for the CONTOP and OONTOP interfaces after adsorption respectively. The Y-axis is labelled as electrostatic potential in eV and the X-axis shows the distance along the Z-direction in Å. Fig. 4.9 and 4.11 show the magnified average electrostatic potential plots for CONTOP and OONTOP interfaces respectively. The change in the electrostatic potential before and after adsorption in TiO_2

can be observed by comparing the magnified average electrostatic potential plots 4.7 with 4.9 and 4.11.

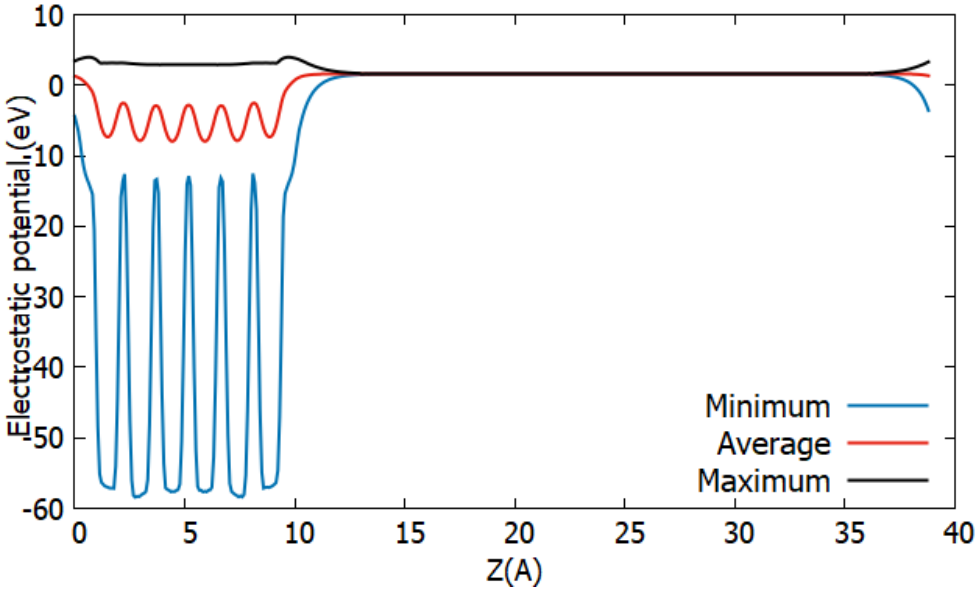

Figure 4.6 Electrostatic potential of surface reconstructed TiO_2 structure: Minimum (blue), Average (red), Maximum (black)

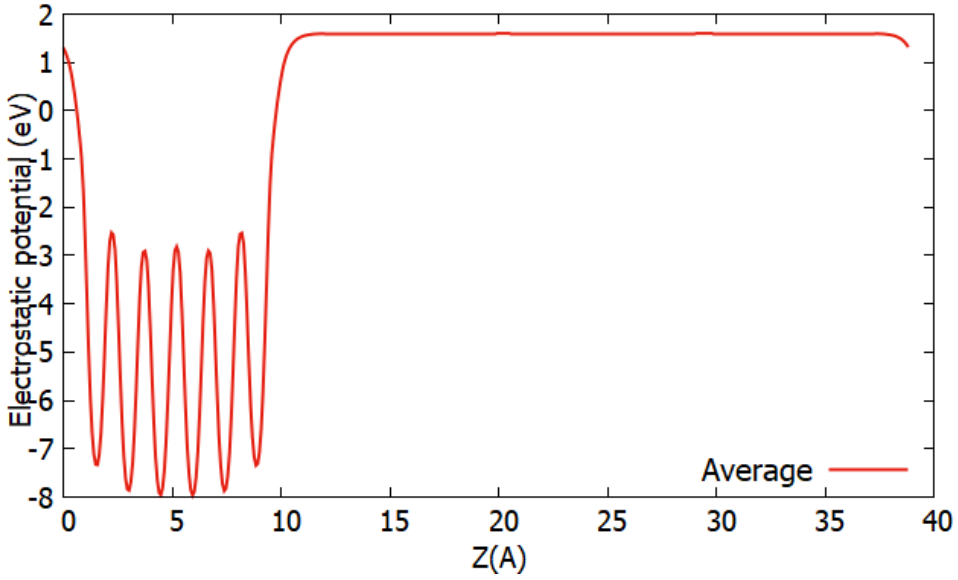

Figure 4.7 The magnified average electrostatic potential of TiO_2 structure (red)

The average electrostatic potential value of TiO_2 before adsorption of the molecule is -4.87 eV. We can see the change in electrostatic potential values of TiO_2 after the adsorption due to interface modification.

Analyzing the average electrostatic potential plots for the adsorbed molecule is very important in order to understand the effects of adsorption and electronic properties of the system. It can be observed from the plots 4.9 and 4.11 that the average electrostatic potential of monolayer lies above the average potential value for TiO_2 at both of the interfaces. For the CONTOP/TiO_2 interface, the average potential for TiO_2 is at -4.266 eV and the average potential of monolayer lies at 0.68 eV. From which we get the net potential difference of 4.946 eV in case of CONTOP/ TiO_2 interface. In the case of OONTOP/TiO_2 interface, the TiO_2 average potential is at -4.537 and the monolayer has the average potential of 0.86 which gives the net potential difference value of 5.397 eV. At both of the interfaces, the net potential difference values are positive.

This concludes that there is a significant potential drop between the monolayer and TiO_2 interface, thus enough driving force is present for the transfer of charge from the monolayer into TiO_2 [37]. These results support the claim of having better charge transfer at the TiO_2/Perovskite interface due to incorporation of 4-mercaptobenzoic acid [14]. As we discussed in the literature review section the interface between TiO_2/Perovskite has a similar profile of the electrostatic potential drop which is the reason for the charge transfer [6] [38]. The electrostatic potential plots for perovskite/HOOC-Ph-SH shows the step increase in the potential from perovskite to monolayer as published in the literature [46]. In this study, the average electrostatic potential of perovskite lies around -2.44 eV and the monolayer has the average potential of 2.44 eV. Considering these results, we get the net

potential difference between perovskite and TiO_2 with monolayer incorporation equal to 1.826 eV which is positive. Thus, there is enough driving force for the electron injection from perovskite to TiO_2 with the step of monolayer potential. We discussed in the literature review part how this step-in electrostatic potential will passivate the trap states and improve the charge transfer by limiting the electron-hole recombination.

	CONTOP/ TiO_2	**OONTOP/ TiO_2**
TiO_2 average potential (eV)	-4.266	-4.537
Monolayer average potential(eV)	0.68	0.86
Net potential difference(eV)	4.946	5.397

Table 2 Average electrostatic potential values of TiO_2 and the monolayer interfaces

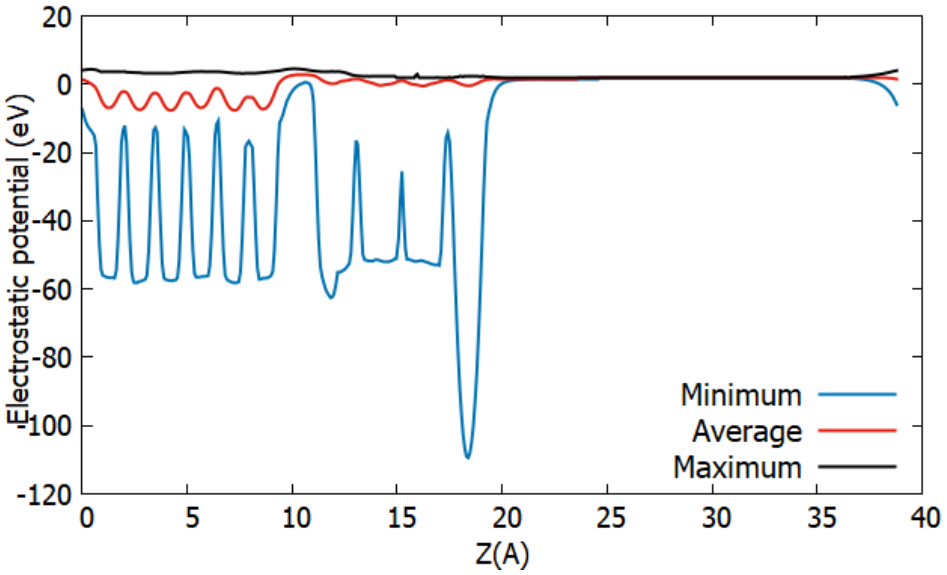

Figure 4.8 Electrostatic potential of optimized TiO_2/HOOC-Ph-SH(CONTOP) interface: Minimum (blue), Average (red) and Maximum (black)

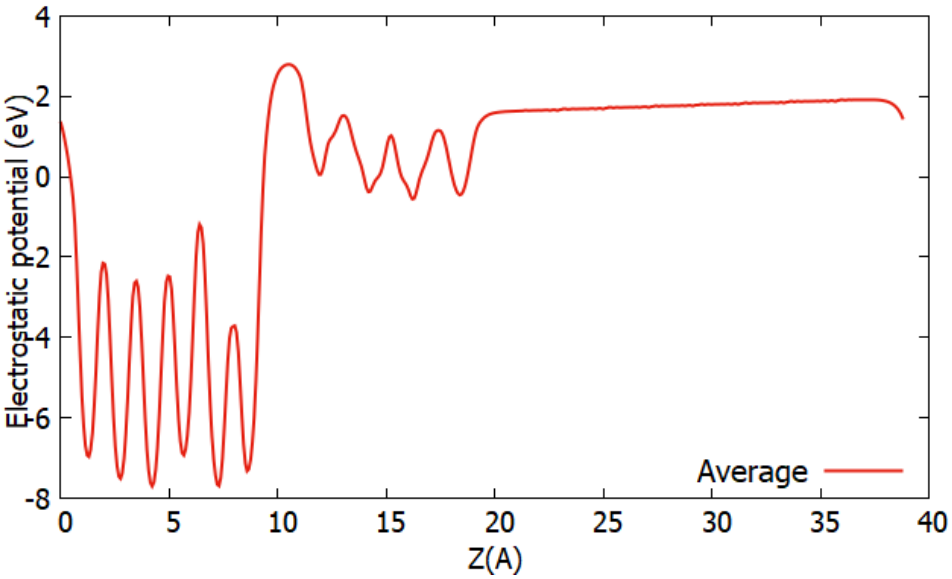

Figure 4.9 Magnified average electrostatic potential of TiO_2/HOOC-Ph-SH(CONTOP) interface

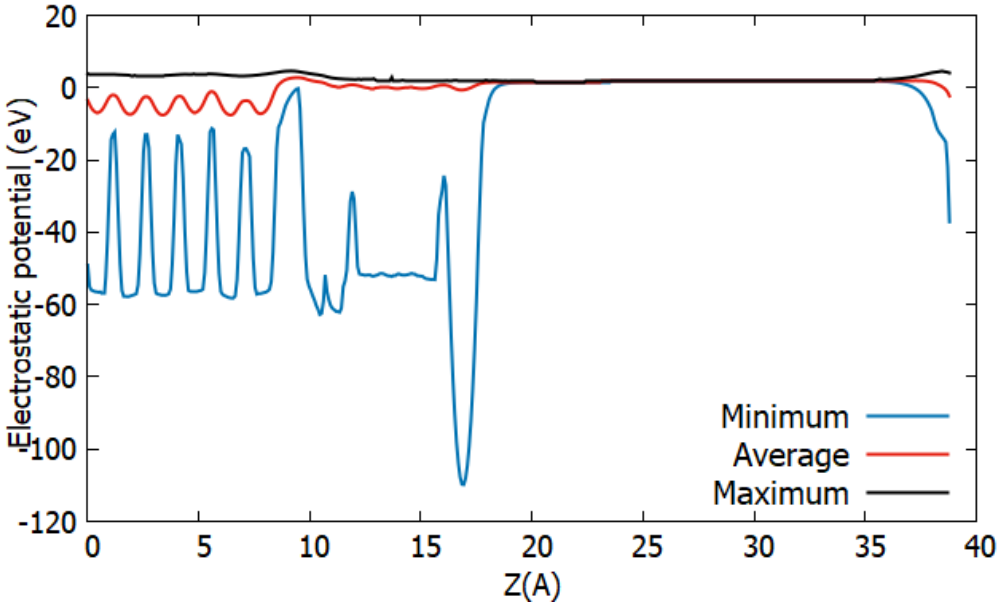

Figure 4.10 Electrostatic potential of TiO_2 /HOOC-Ph-SH(OONTOP): Minimum (blue), Average (red) and Maximum (black)

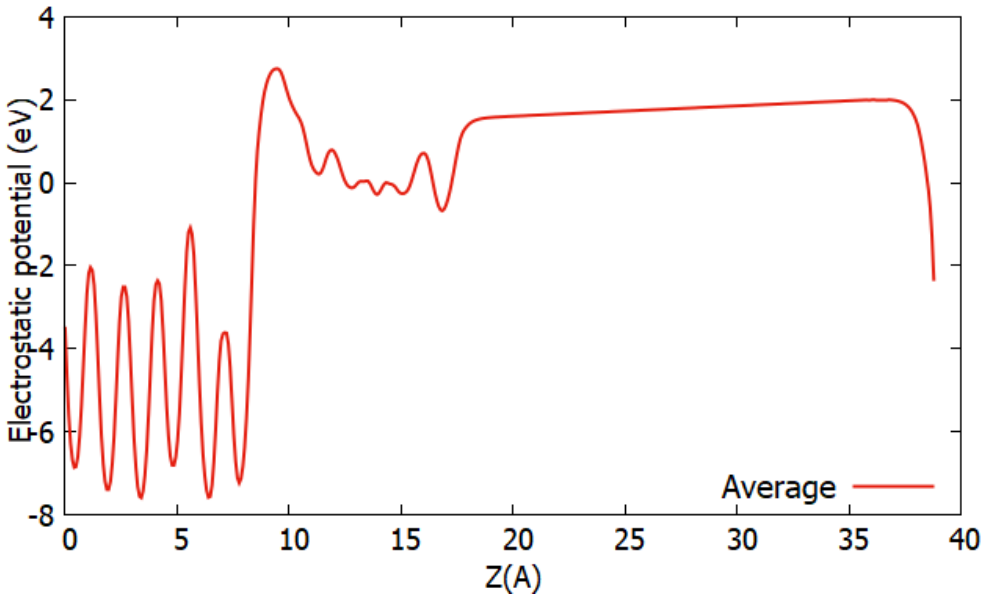

Figure 4.11 Magnified average electrostatic potential of TiO_2/HOOC-Ph-SH(OONTOP) interface

Also, the higher the potential drop at the interface, the better would be the charge redistribution at the interface which will help inhibit the separated charge recombination [6]. This inhibition of recombination losses improves overall cell performance. Average electrostatic potential values for both of the interfaces are presented in table 2. The net potential difference between TiO_2 and the monolayers are 4.946 and 5.397 respectively. This potential difference is the major driving force for the charge transfer from monolayer to TiO_2.

4.6 Charge density analysis

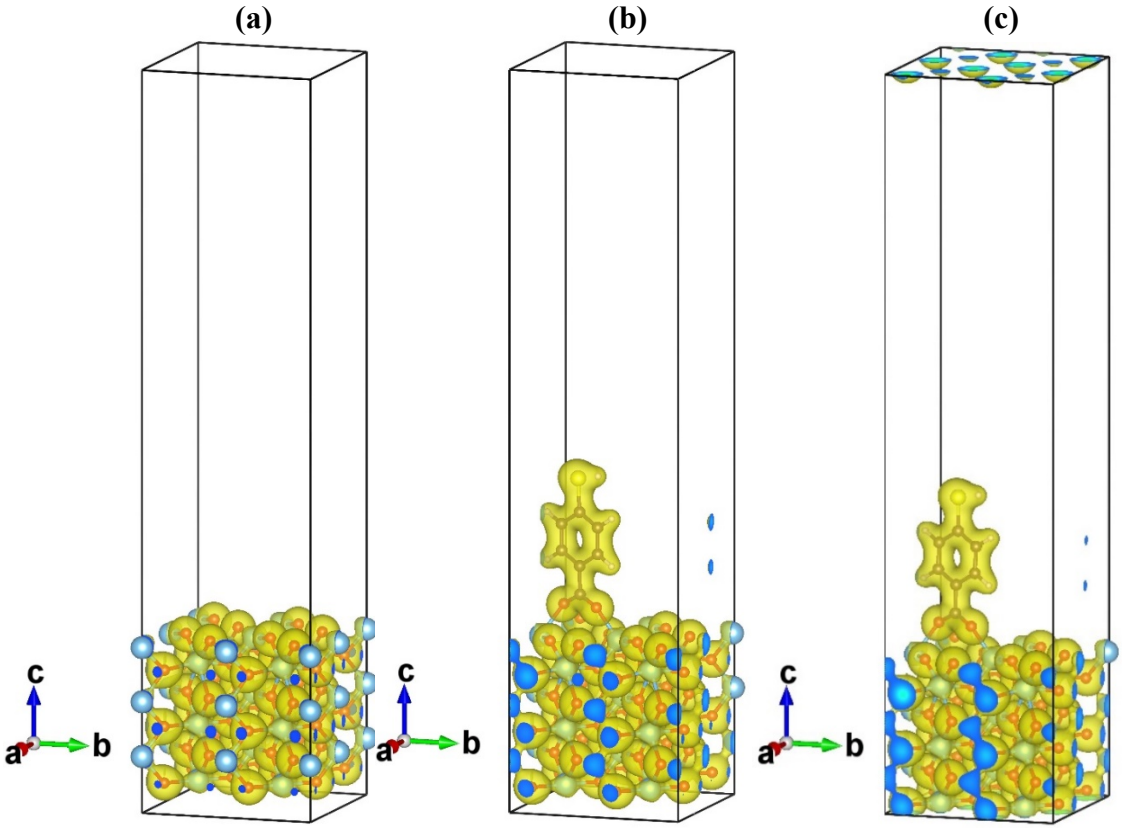

Figure 4.12 a) charge density of surface reconstructed TiO_2 b) charge density of TiO_2 /HOOC-Ph-SH(CONTOP) interface (c) charge density of TiO_2/HOOC-Ph-SH (OONTOP)

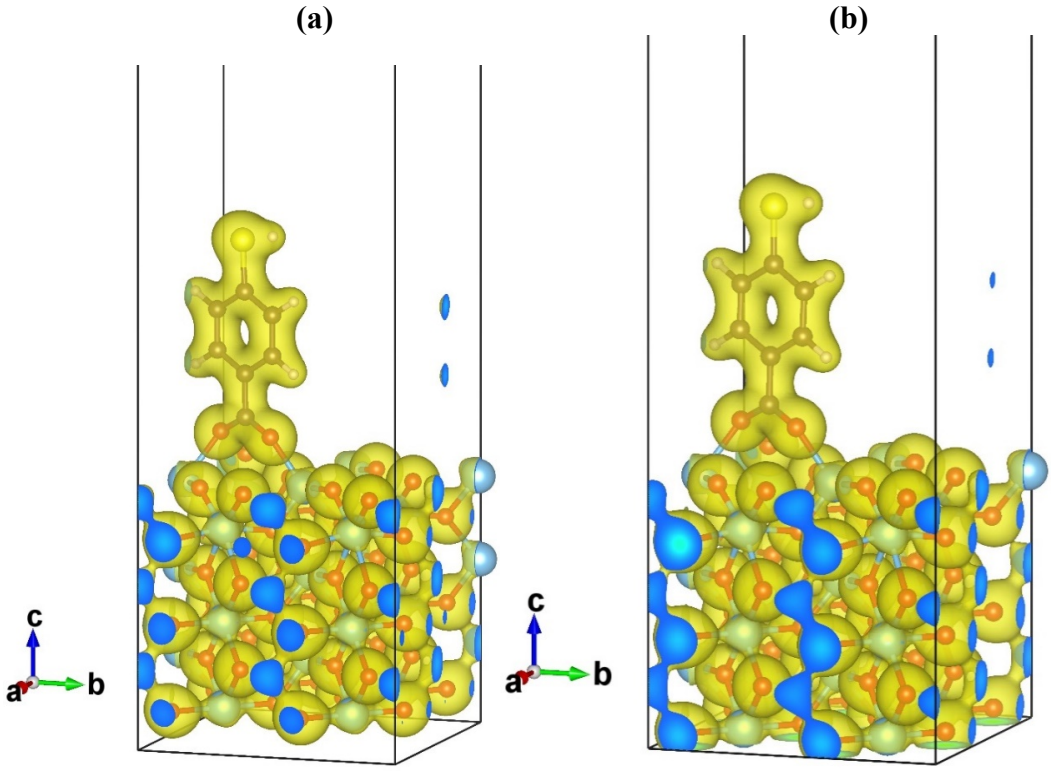

Figure 4.13 Magnified charge density plots for the (a) TiO_2/HOOC-Ph-SH(CONTOP) and (b) TiO_2 /HOOC-Ph-SH(OONTOP)

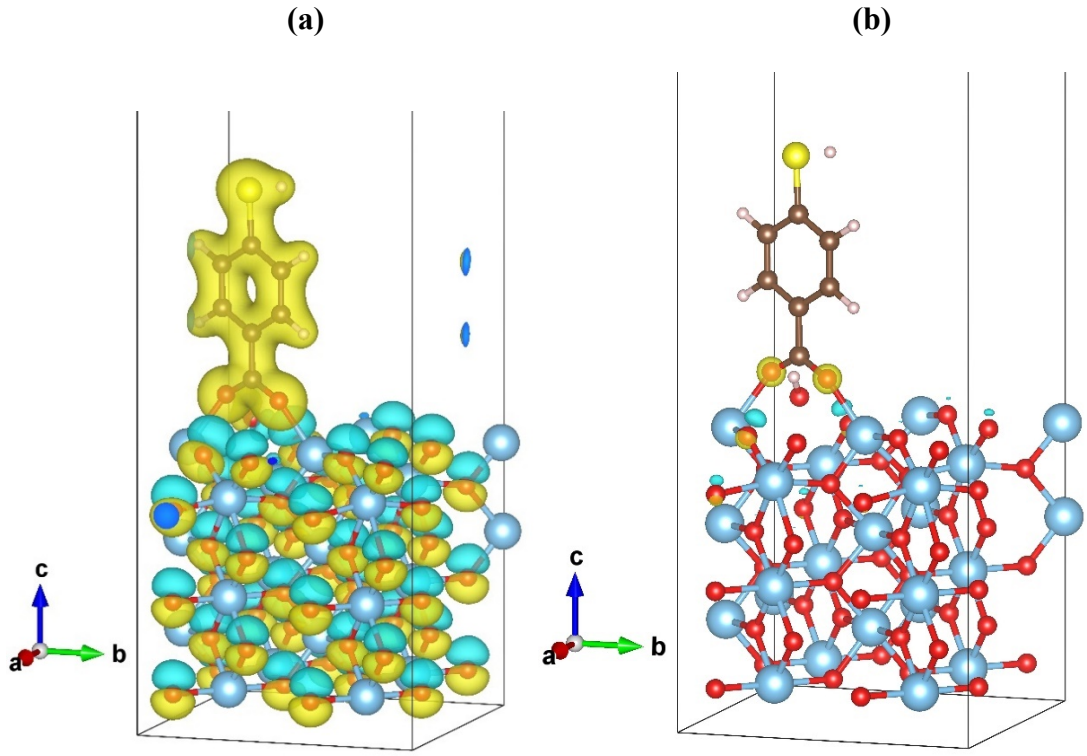

Figure 4.14 charge density difference plot of TiO_2/HOOC-Ph-SH(CONTOP) with (a) threshold 0.06 and b) with 0.55 threshold

The charge density plots of the surface reconstructed titanium dioxide and both of TiO_2/HOOC-Ph-SH interfaces are shown in Fig. 4.12. Fig. 4.13 shows the magnified view of the charge density in order to study the charge distribution at the interface before and after adsorption. The threshold values for all the structures are kept constant at 0.060 (electron/$Bohr^3$) to show fair comparison. Minimum, maximum and threshold values of the charge densities are presented in table 3. The maximum and minimum charge density values for TiO_2 range from -1.033 to 1.211 and for TiO_2/molecule values range from -0.042 to 1.225. Magnified charge density distribution plot for both the 'CONTOP' and 'OONTOP' interfaces are very similar to each other hence approximately the same amount of charge distribution can be seen in both cases.

Charge density(e/bohr^3)	Surface reconstructed TiO_2	TiO_2/HOOC-Ph-SH(CONTOP)	TiO_2/HOOC-Ph-SH(OONTOP)
Threshold	0.06	0.06	0.06
Minimum	-1.033	-0.042	-0.042
Maximum	1.211	1.225	1.225

Table 3 Charge density threshold values

To further analyze the electronic properties of the interface we have calculated the charge density difference plots, obtained by subtracting the charge density of TiO_2 reconstructed surface from the charge density of the surface with monolayer adsorbed, for the 'CONTOP' interface as shown in Fig. 4.14. After increasing the threshold value to 0.55, we can identify the positive/negative charge redistribution at the interface. The blue color represents the charge depletion whereas the yellow color represents the charge accumulation. This charge distribution at the interface results in the electric dipole formation. The formation of the dipole at the interface supports band bending and band edge alignment which helps in better charge transfer as stated in the literature [6].

4.7 Interface charge alteration upon monolayer adsorption

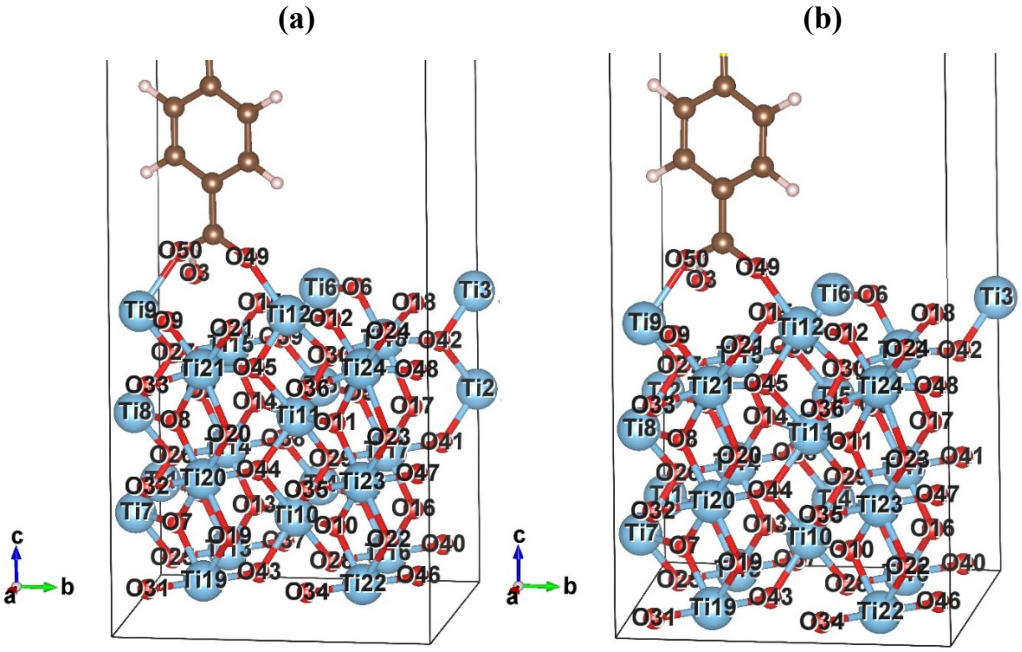

Figure 4.15 (a) CONTOP interface with numbered atoms (b) OONTOP interface with numbered atoms

Atoms (CONTOP)	Charge after adsorption	Charge before adsorption	Charge difference	Atoms (OONTOP)	Charge After adsorption	Charge before adsorption	Charge difference
Ti_8	4.201	4.318	-0.117	**Ti_8**	4.199	4.318	-0.119
Ti_9	4.278	4.413	-0.135	**Ti_9**	4.274	4.413	-0.139
Ti_{12}	4.238	4.413	-0.175	**Ti_{12}**	4.239	4.413	-0.174
Ti_{15}	4.204	4.025	0.179	**Ti_{15}**	4.202	4.025	0.177
O_3	5.093	4.974	0.119	**O_3**	5.093	4.974	0.119
O_{49}	5.14	5.125	0.015	**O_{49}**	5.14	5.125	0.015
O_{50}	5.136	5.16	-0.024	**O_{50}**	5.135	5.16	-0.025

Table 4 charge values of some of the selected atoms before and after adsorption

To further analyze the charge distribution at the interface atoms, we have calculated the total charge values on some of the atoms with major charge difference before and after adsorption of the monolayer. Fig. 4.15 a) and b) shows the monolayer adsorbed

onto TiO_2 with numbered atoms for both the 'CONTOP' and 'OONTOP' interfaces respectively. The respective charge values are tabulated in table 5.

At both of the interfaces, the total charge differences are quite similar with the same signs. The interface atom Ti_9 and Ti_{12} have shown the negative value of charge difference which means it has lost some of its charges after adsorption. This is due to the bonding of Ti atom with Oxygen, as we know Oxygen has high electronegativity thus the shared electrons are more leaned towards the oxygen atoms. In case of Ti_8 atom which lies bellow the interface at the 3rd layer, the charge difference is negative which is because the atom is coordinated with the other oxygen atoms with bonds to Ti_9. Whereas, in case of Ti_{15}, which lies at the interfacial surface the charge difference value is positive as the atom undercoordinated because of the O atom attached to it before adsorption detaches and reattaches to the hydrogen atom.

When we consider the O_3 atom at the interface, it can be seen that it gained some major charge after adsorption. This is because it breaks one of the bonds with Ti_{15} and reattaches to the hydrogen atom detached from the monolayer. O_{49} and O_{50} are the atoms which belong to monolayer and have directly attached to the TiO_2 surface thus the O_{49} shows a minute gain in charge due to attachment with TiO_2, whereas O_{50} has seen to lose a little amount of charge which is due to the detachment of the hydrogen atoms from it. The new bond lengths formed between Ti – O are 2.05 and 2.06 which are very close to the bond length between Ti and O which is 1.98 Å. These results strongly support that the interaction among these atoms is through covalent bonding.

4.8 Electron localization function

Since the interaction among the atoms at the interface is important to analyze the charge transfer mechanism, we have plotted 2-D representations of the electron localization function using VESTA for surface reconstructed TiO_2, and both of the interfaces as shown in Fig. 4.15(a), (b) and (c) respectively. Electron localization function is a reliable method for identifying the type of bonding present in the system.

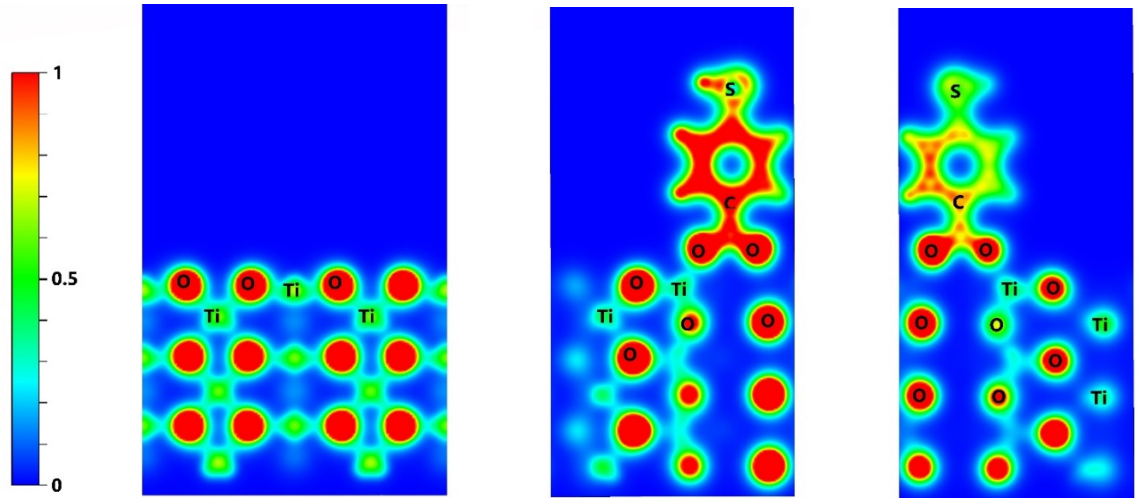

Figure 4.16 electron localization function of (a) surface reconstructed TiO_2 (b) TiO_2/HOOC-Ph-SH(CONTOP) interface (b) TiO_2/HOOC-Ph-SH(OONTOP) interface

ELF plots depict the probability of finding an electron at a particular location. The value of ELF plots ranges from 0 to 1, 1 being the highly localized electrons and 0 being no localization. The value of 0.5 of localization corresponds to the electron-gas like feature which indicates the presence of covalent nature between the atoms. Here, the blue color region corresponds to no localization, red color represents highly localized electrons and the green color corresponds to electron gas like characteristics. As seen in Fig. 4.16 b) and c), the region around Ti and O atoms connected at the interface is green and shows the

electron gas like feature. This region represents the overlap of electron orbitals at the interface which is an indication of the formation of a covalent bond. This chemical interaction at the interface supports better charge transfer from the molecule into TiO_2.

4.9 Total and Partial density of states

The density of states describes the number of states available in the system at each energy level which helps in determining the carrier concentration and charge distribution of the system. Fig. 4.17 shows the total density of states as well as the partial density of states for surface reconstructed TiO_2. The total density of states is represented by the black outer line. PDOS plot of the TiO_2 is compared to the results published in the literature [44] which follows the similar pattern of the energy band occupancies. Here we can see that the valence band is mainly occupied by the Oxygen *p*-orbital whereas the conduction band is mainly occupied by the titanium *d*-orbitals. All the Ti-*s*, Ti-*p* and Ti-*d* orbitals contribute to the total density of states, whereas Ti-*d* contribution is significant compared to *s* and *p* orbitals. From the PDOS it is concluded that the excess electrons occupy the Ti-*d* orbitals whereas the excess holes occupy the O-*p* orbitals.

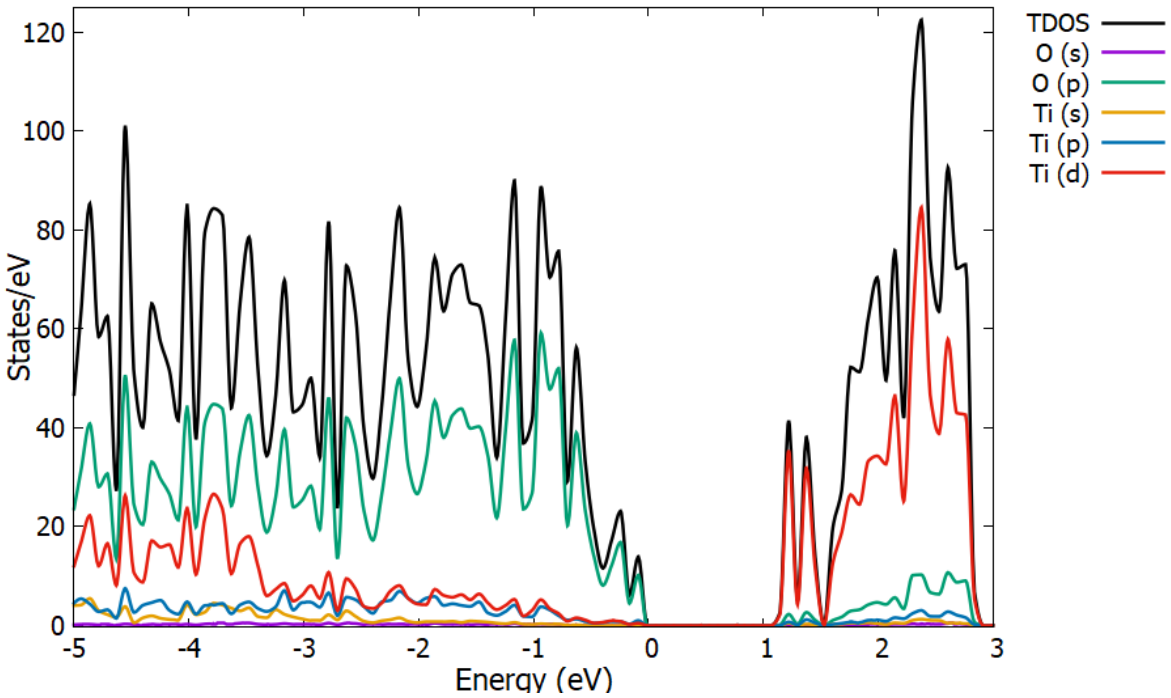

Figure 4.17 Total density of states (TDOS) and partial density of states with the elemental contribution of TiO_2

The total and partial density of states of TiO_2/monolayer (CONTOP) and TiO_2/monolayer (OONTOP) interfaces are also plotted to analyze the effects of adsorption on TiO_2 as shown in Fig. 4.18 and 4.19 respectively. It can be seen from all the plots that the bandgap of all the structure remains approximately the same which is equal to 1.1 eV thus the bandgap energy remains in the range suitable for solar cell applications, which bolsters the results that the monolayer is not harming the interface light absorption characteristics.

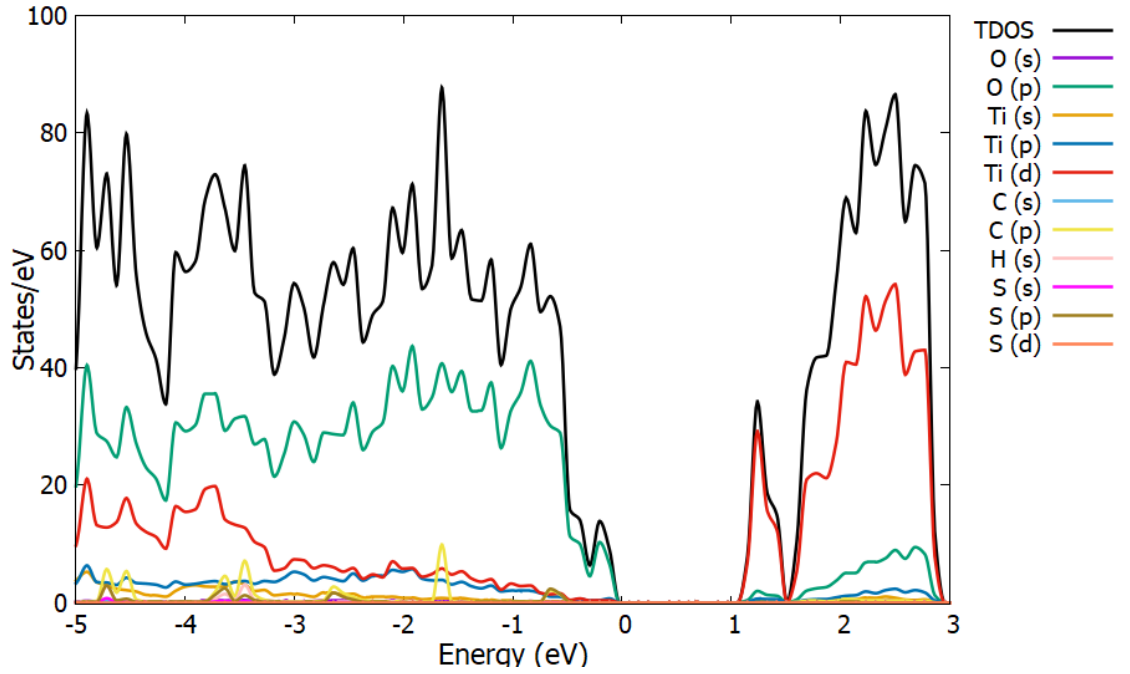

Figure 4.18 Total density of states (TDOS) and partial density of states with the elemental contribution of TiO_2/Monolayer (CONTOP) interface

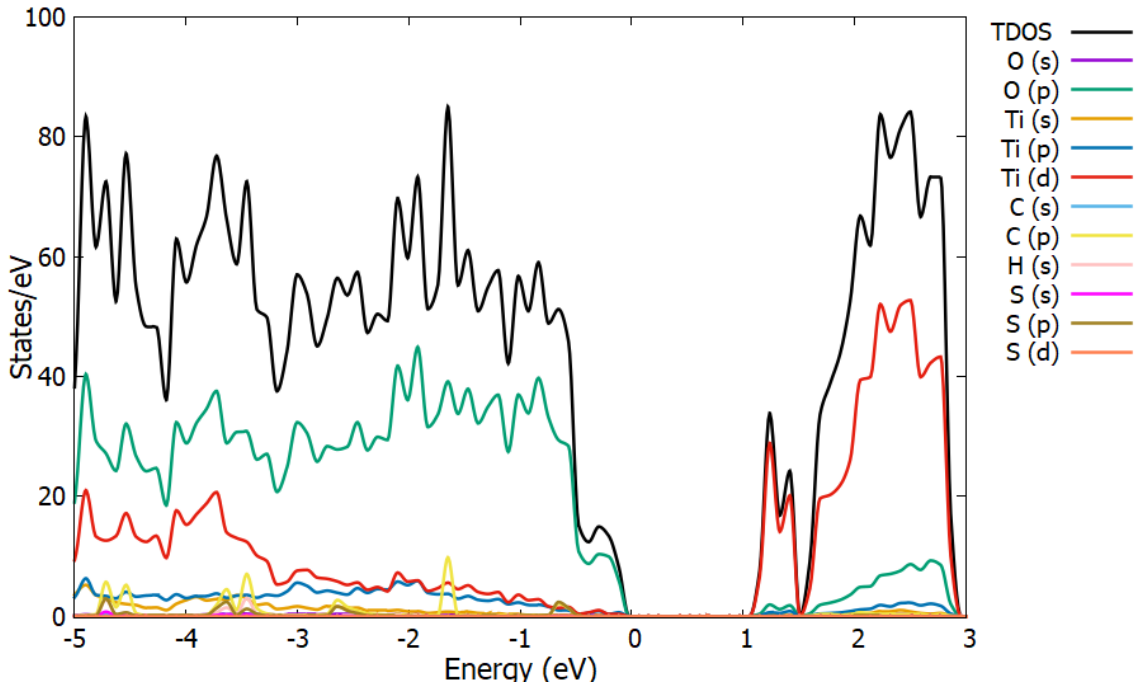

Figure 4.19 Total density of states (TDOS) and partial density of states with the elemental contribution of TiO_2/monolayer (OONTOP) interface

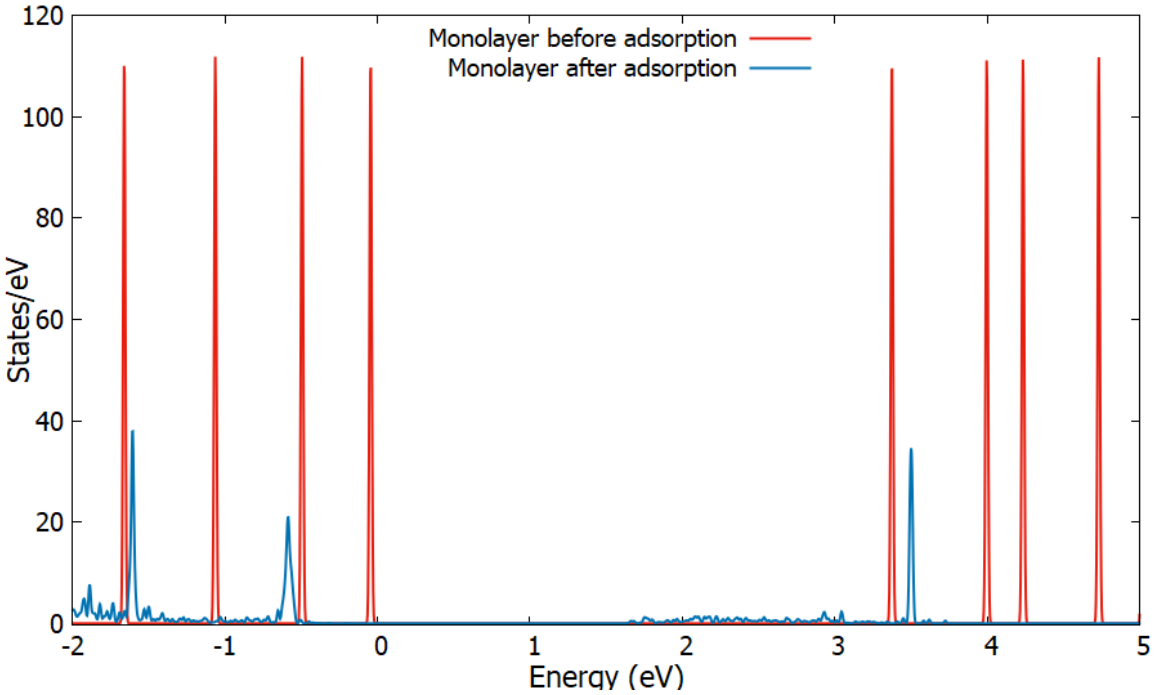

Figure 4.20 DOS comparison of the molecule before and after adsorption

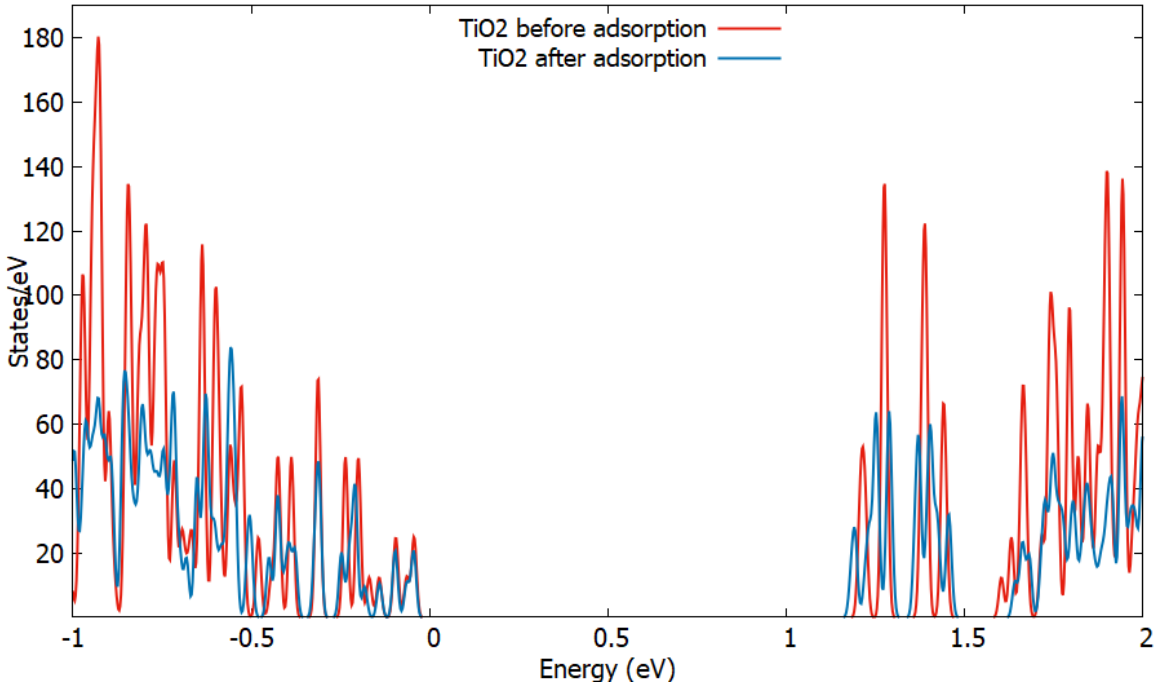

Figure 4.21 DOS comparison of TiO_2 before and after adsorption

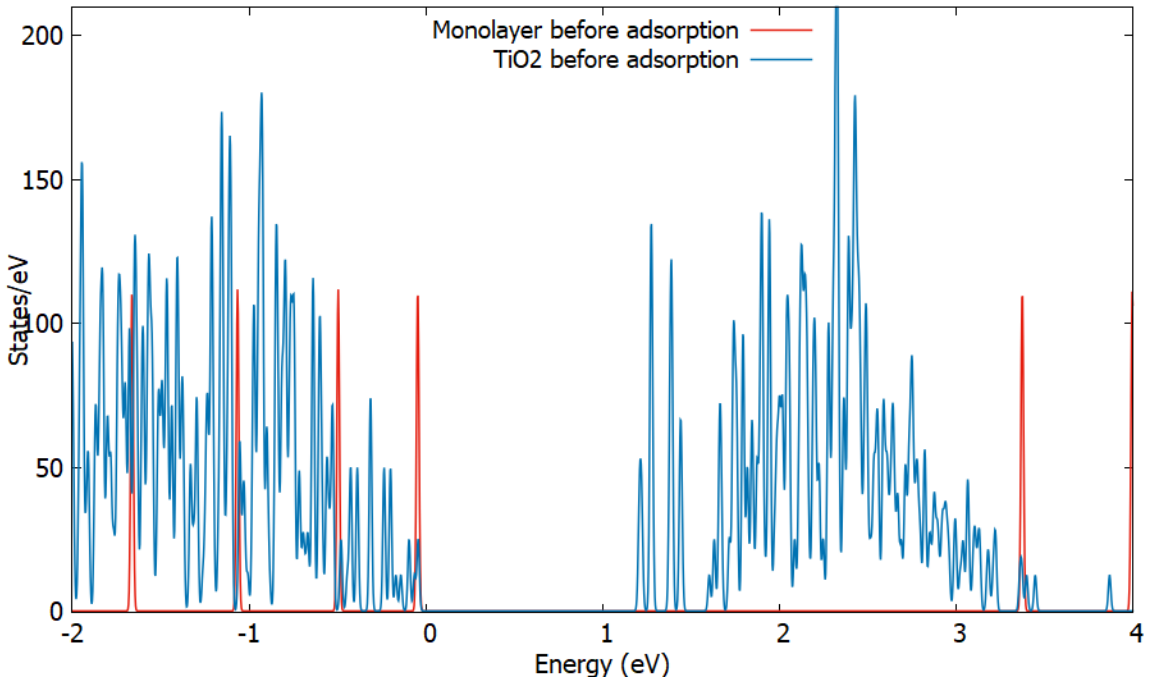

Figure 4.22 Comparing DOS of TiO_2 and Molecule before adsorption

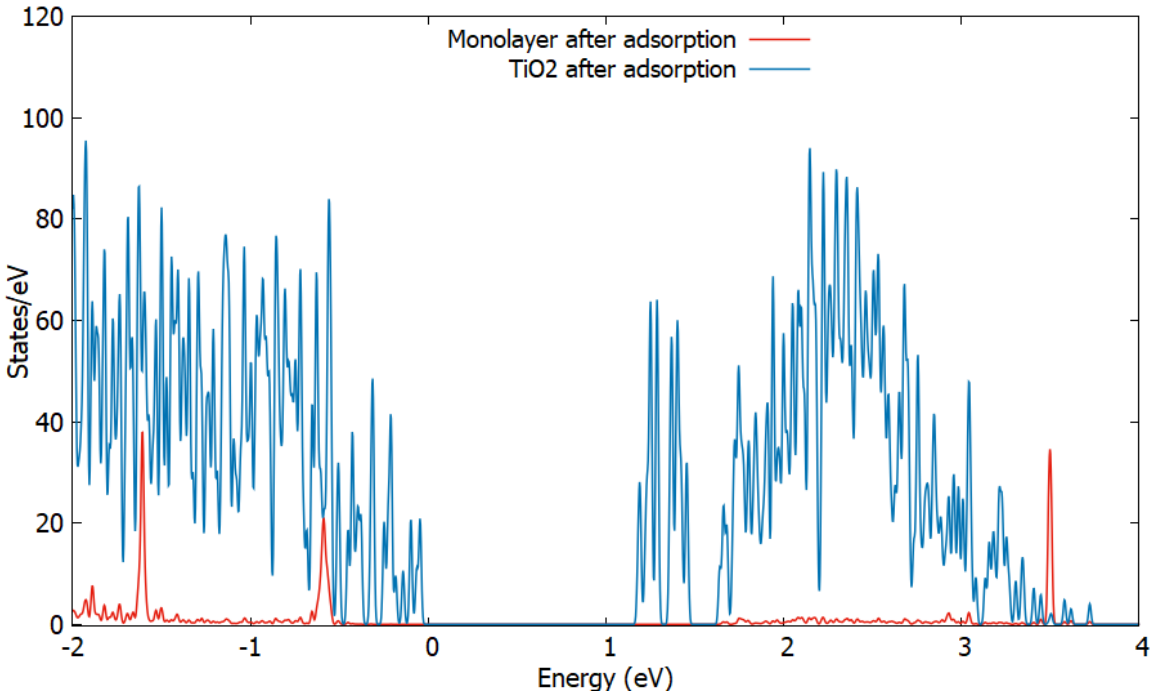

Figure 4.23 Comparing DOS of TiO_2 and Molecule after adsorption

To further analyze the partial density of states we have plotted the density plots near the bandgap range with higher data points in order to investigate the change in states

near the Fermi energy level. Fig. 4.20 and 4.21 shows the comparison between the density of states of the monolayer and TiO_2 respectively before and after adsorption.

Fig. 4.22 shows the DOS plots for TiO_2 and molecule combined in the same plot before adsorption. We can see that the DOS of TiO_2 shows larger peak values for the states before adsorption, however, these peaks have reduced and broader conduction and valence bands are generated after adsorption as shown in Fig. 4.23. Also, for the molecule as well we can see the longer peaks before adsorption which are broadened after the adsorption.

There is no significant change in the bandgap of the system and remains same after adsorption which is a good indication that no adverse effect is caused by the adsorbed molecule, as the bandgap remains in the absorption range for the photovoltaic applications.

The alignment of LUMO-HOMO level of the molecule with respect to bands of TiO_2 is an important factor affecting the performance of the solar cell as it determines the effectiveness of electron injection and recombination of the separated charges [42] [43] [44]. The LUMO level of the molecule has to be at higher energy than the conduction band edge of TiO_2 for generating the required driving force for effective electron injection. Also, the LUMO of the molecule is coupled with the conduction band of TiO_2 hence the overlap between these energy states is desirable for better charge transfer. It is worth noting that, the LUMO of the molecule is at a higher level than the CBM of TiO_2, this large gap in these energy levels will provide a large driving force for electron injection hence ensures effective charge transfer at the interface.

After adsorption, we can see the accumulated states in the lowest unoccupied molecular orbitals (LUMO) of the molecule, which reduces the bandgap of the molecule as seen in Fig. 4.22. Also, the bandgap of the molecule is wider than that of TiO_2 (HOMO

of molecule lies bellow the VBM of TiO_2 and LUMO of the molecule lies above the CBM of TiO_2) which prevents the recombination of the separated charge, which is responsible for the improved efficiency of an overall solar cell. The accumulation of new states in the LUMO of the molecule indicates the effective charge transfer across the interface.

In order to check the stability of the molecule, we have calculated the adsorption energy of the molecule adsorbed on TiO_2 (CONTOP). The adsorption energy is defined as [44]

$$E_{ads} = E_{molecule/TiO_2} - (E_{molecule} + E_{TiO_2}) \quad (4.1.1)$$

$$E_{ads} = -614.191\ eV - (-520.600\ eV - 91.098\ eV)$$

$$E_{ads} = -2.491\ eV$$

Here, $E_{molecule/TiO_2}$ is the total energy of the adsorbed system, $E_{molecule}$ is the energy of the fully relaxed isolated monolayer and E_{TiO_2} is the energy of the adsorbent supercell. From the above equation, we get a negative value for the energy of adsorption which is considered as the stable adsorption.

CHAPTER 5 CONCLUSION

We have used an ab initio quantum mechanical approach to analyze various structural and electronic properties of the TiO_2/HOOC-Ph-SH interface in order to understand the charge transfer and atomic interactions among atoms at the interface. The motivation was experimental results from the literature that the incorporation of 4-mercaptobenzoiac acid (HOOC-Ph-SH) monolayer between perovskite/ETL interface improves the power conversion efficiency of hybrid perovskite solar cells.

Our results show that the average electrostatic potential of the monolayer lies above the TiO_2 thus it is more favorable for the electrons to inject from monolayer into TiO_2. Moreover, the interaction of the atoms at the interface is through strong covalent bonding which helps in effective charge transfer as well as providing flexibility and support to the overall cell. The redistribution of the charges due to the formation of electric dipoles at the interface results in band bending that assist in effective charge transfer. The density of states plots indicates that the LUMO level of the monolayer lies within the conduction band of the TiO_2 such that there is enough driving force available for the effective electron injection from monolayer into TiO_2. Furthermore, the negative adsorption energy supports the stable adsorption of the monolayer onto TiO_2. Considering the results of the previously published literature it is seen that the monolayer forms a step-in potential which may act as a potential barrier, thus allowing the effective electron transfer and blocking the back transfer of holes. From these results, it can be concluded that the adsorption of the monolayer is an effective approach to passivate the trap states and facilitate the charge transfer at the perovskite/ETL interface that result in improving power conversion efficiency.

REFERENCES

[1] https://en.wikipedia.org/w/index.php?title=Photoelectric_effect&oldid=941058368.

[2] S. Sharma, K.K. Jain and A. Sharma, Solar Cells: In Research and Applications—A Review. Materials Sciences and Applications, 6, 1145-1155 (2015).

[3] Martin A. Green, Anita Ho-Baillie and Henry J. Snaith, The emergence of perovskite solar cells. Nature Photonics, vol 8, 506-514, (July 2014).

[4] Nam Gyu-park. Perovskite solar cells: an emerging photovoltaic technology, Materials Today, Volume18, Number 2, 65-72 (March 2015).

[5] Arianna Marchioro, Joel Teuscher, Dennis Friedrich, Marinus Kunst, Roel van de Krol, Thomas Moehl, Michael Gratzel and Jacques-E. Moser, Unravelling the mechanism of photo-induced charge transfer processes in lead iodide perovskite solar cells. Nature Photonics, Vol 8, 250-255 (March 2014).

[6] Wei Geng, Chuan-Jia Tong, Jiang Liu, Wenjun Zhu, Woon-Ming Lau, and Li-Min Liu, Structures and Electronic Properties of Different CH3NH3PbI3/TiO_2 Interface: A First-Principles Study. Scientific reports, 6:20131, 1-8 (2015).

[7] Y. Wang, J. Wan, J. Ding, J. Hu and D. Wang, A rutile TiO_2 electron transport layer of Charge collection for Efficient Perovskite Solar cells. angew. Chem. Int. Ed. 58, 9414-9418 (2019).

[8] J. W. Lee, T. Y. Lee, P. J. Yoo, M. Gratzel, S Mhaisalkar and N. G. Park, Rutile TiO_2 based perovskite solar cells. J.Mater. Chem. A, 2, 9251-9259 (2014).

[9] T. T. H. Tran, H. Cosslick, A. Schulz, Q. L. Nguyen, Photocatalytic performance of crystalline titania polymorphs in the degradation of hazardous pharmaceuticals and dyes, Adv. Nat. Sci.: Nanosci. Nanotechnol. **8** (2017) 015011

[10] A. Yella, L. P. Heiniger, P. Gao, M. K. Nazeeruddin and M. Gratzel, Nanocrystalline rutile electron extraction layer enables low-temperature solution-processed perovskite photovoltaics with 13.7 % Efficiency. pubs.acs.org/Nano. Let. 14, 2591-2598 (2014).

[11] Ulrike Diebold, The surface science of titanium dioxide. Elsevier, surface science reports 48, 53-229 (2003).

[12] F. Labat, P. Baranek, and C. Adamo, Structural and Electronic properties of selected rutile and anatase TiO_2 surface: An ab initio investigation. J. Chem. Theory Comput. 4, 341-352 (2008).

[13] A. Huang, L. Lei, J. Zhu, Y. Yu, Y. Liu, S. Yang, S. Bao, X. Cao, and Ping jin, Achieving High Current Density of Perovskite Solar Cells by Modulating the Dominated Facets of Room-Temperature DC Magnetron Sputtered TiO_2 Electron Extraction Layer. ACS Appl. Mater. Interfaces 9, 2016−2022 (2017).

[14] Jing Cao, Jun Yin, Shangfu Yuan, Yun Zhao, Jing L and Nanfeng Zheng, Thiols as interfacial modifiers to enhance the performance and stability of perovskite solar cells. Nanoscale, 7, 9443–9447 (2015).

[15] F.A. Grant, Properties of rutile (Titanium Dioxide). Reviews of modern physics. Vol. 31, number 3. 646-674 (July 1959).

[16] Khalid Mahmood, Saad Sarwar and Muhammad Mehran, Current status of electron transport layers in perovskite solar cells: materials and properties. RSC Adv. 7, 17044–17062 (2017).

[17] Yang Bai, Xiangyue Meng and Shihe Yang, Interface Engineering for Highly Efficient and Stable Planar p-i-n Perovskite Solar Cells. Adv. Energy Mater. 8, 1701883. 1-14 (2017).

[18] Gill Sang Han, Hyun Suk Chung, Byeong Jo Kim, Dong Hoe Kim, Jin Wook Lee, Bhabani Sankar Swain, Khalid Mahmood, Retarding charge recombination in perovskite solar cells using ultrathin MgO-coated TiO_2 nanoparticulate films. J. Mater. Chem. A, 3, 9160–9164 (2015).

[19] Seigo Ito, Soichiro Tanaka, Kyohei Manabe and Hitoshi Nishino, Effects of Surface Blocking Layer of Sb2S3 on Nanocrystalline TiO_2 for $CH_3NH_3PbI_3$ Perovskite Solar Cells. J. Phys. Chem. C, 118, 16995−17000 (2014).

[20] Jun Peng, Yiliang Wu, Wang Ye, Daniel A. Jacobs, Heping Shen, Xiao Fu, Yimao Wan, The Duong, Nandi Wu, Chog Barugkin, Hieu T. Nguyen, Dingyong Zhong, Juntao Li, Teng Lu, Yun Liu, Interface passivation using ultrathin polymer–fullerene films for high-efficiency perovskite solar cells with negligible hysteresis. *Energy Environ.* Sci., 10, 1792—1800 (2017).

[21] Xiaolei Zhang, Zhi Yu, Wei Ji, Huimin Sui, Qian Cong, Xu Wang and Bing Zhao, Charge-Transfer Effect on Surface-Enhanced Raman Scattering (SERS) in an Ordered Ag NPs/4-Mercaptobenzoic Acid/TiO_2 System. J. Phys. Chem. C, 119, 22439−22444 (2015).

[22] Juan Dong, Jiangjian Shi, Dongmei Li, Yanhong Luo, and Qingbo Meng, Controlling the conduction band offset for highly efficient ZnO nanorods based perovskite solar cell. Appl. Phys. Lett. 107, 073507. 1-5 (2015).

[23] Jun-Yuan Jeng, Yi-Fang Chiang, Mu-Huan Lee, Shin-Rung Peng, Tzung-Fang Guo, Peter Chen and Ten-Chin Wen, $CH_3NH_3PbI_3$ Perovskite/Fullerene Planar-Heterojunction Hybrid Solar Cells. Adv. Mater. 25, 3727–3732 (2013).

[24] Wataru Okada, Takeo Suga, Kenichi Oyaizu, Hiroshi Segava and Hiroyuki Nishide, Perovskite/TiO_2 interface passivation using poly (vinyl carbazole) and fullerene for the photo-conversion efficiency of 21%. ACS Appl. Energy mater. 2,4, 2848-2853 (2019).

[25] Gaurav Kapil, Teresa Ripolles, Kengo Hamada, Yuhei Ogomi, Takeru Bessho, Highly Efficient 17.6% Tin-lead mixed perovskite solar cells realized through spike structure. Nano Lett. 18, 3600−3607 (2018).

[26] Zhiqi Li, Jiajun Dong, Chunyu Liu, Jiaxin Guo, Liang Shen, Wenbin Guo, Surface Passivation of Perovskite Solar Cells Toward Improved Efficiency and Stability. Nano-Micro Lett. 11:50 (2019).

[27] G. Kresse and J. Hafner. “Ab initio molecular dynamics for liquid metals”. Phys. Rev. B, **47**,558 (1993).

[28] G. Kresse and J. Hafner. “Ab initio molecular dynamics simulation of the liquid-metalamorphous-semiconductor transition in germanium”. Phys. Rev. B, **49**, 14251 (1994).

[29] G. Kresse and J. Furthmu¨ller. “Efficiency of ab-initio total energy calculations for metals and semiconductors using a plane-wave basis set”. Comput. Mat. Sci., 6-15 (1996).

[30] G. Kresse and J. Furthmu¨ller. “Efficient iterative schemes for ab initio total-energy calculations using a plane-wave basis set”. Phys. Rev. B, **54**, 11169 (1996).

[31] David S. Sholl, Janice A. Steckel, Density functional theory a practical introduction, a john Wiley % sons, Inc., publication, (2009).

[32] P. Hohenberg and W. Kohn, Inhomogeneous Electron Gas, Phys. Rev. 136, B 864-871 (1964).

[33] W. Kohn and L. J. Sham, Self-Consistent Equations Including Exchange and Correlation Effects, Phys. Rev. 140, 1133-1138 (1965).

[34] A. Hossain, Introduction to density functional theory, Department of Physics and Astronomy, University of British Columbia, Vancouver, Canada (2004).

[35] https://cms.mpi.univie.ac.at/vasp/vasp/vasp.html

[36] K. Edgecombe, A. Becke, A simple measure of electron localization in atomic and molecular systems, American Institute of Physics, 92, 5397-5403, (1990).

[37] N. Pham, N. Vu, V. Pham, H. Ta, T. Cao, N. Thoi, Comprehensive resistive switching behaviour of hybrid polyvinyl alcohol and TiO_2 nanotube nanocomposites identified by

combining experimental and density functional theory studies, J. mater. Chem C, 6,1959-1970, (2018)

[38] Z. Yang, Y. Wang, Y. Liu, Stability and charge separation of different $CH_3NH_3SnI_3/TiO_2$ interface: A first-principle study, Applied surface science, 441, 394-400, (2018).

[39] R. Li, H Lv, X. Zhang, P. Liu, L. Chen, J. Cheng, B. Zhao, Vibrational spectroscopy functional theory study of 4-mercaptobenzoic acid, Spectroshimica Acta Part A: Molecular and biomolecular spectroscopy 148, 369-374, (2015).

[40] C. Ho, S. Lee, SERS and DFT investigation of the adsorption behaviour of 4-mercaptobenzoic acid on silver acid on silver colloids, Physicochem. Eng. Aspects 474, 29-35, (2015).

[41] K. Momma and F. Izumi, VESTA: a three-dimensional visualization system for electronic and structural analysis, Appl. Crystallogr., 41, 653-658 (2008).

[42] Mang Niu, The Adsorption Geometry and Electronic Structure of Organic Dye Molecule on TiO_2(101) Surface from First-Principles Calculations, MATEC Web of Conferences 88, 03002 (2017)

[43] L. W. C. Paes, J. Amaya Suárez, A. M. Márquez and Javier. Fdez. Sanz, First-Principles Study of Nickel Complex with 1,3-dithiole-2-thione-4,5-dithiolate Ligands as Model Photosensitizers, Departamento de Ciências Exatas, Escola de Engenharia Industrial e Metalurgia de Volta Redonda, 27255-125

[44] Chundan Lin, Qide Xia, Kuan Li, Juan Li and Zhenqing Yang, Theoretical Study of Ultrafast Electron Injection into a Dye/TiO_2 System in Dye-Sensitized Solar Cells, Journal of the Korean Physical Society, Vol. 72, No. 11, June 2018, pp. 1307- 1312

[45] Charles D. Griego, Karthikeyan Saravanan, John A. Keit, Benchmarking computational alchemy for carbide, nitride, and oxide catalysts, Advanced theory and simulations, 2018

[46] Amlani, Parin Divya, Configuration and Electronic Properties of the Interface between Lead Iodide Hybrid Perovskite and Self assembled Monolayers in Solar Cells, (2017). Browse all Theses and Dissertations. 1868.